Completion of neuronal remodeling prompts myelination along developing motor axon branches

Completion of neuronal remodeling prompts myelination along developing motor axon branches

Mengzhe Wang[1], Tatjana Kleele[1, 10], Yan Xiao[1], Gabriela Plucinska[1, 11], Petros Avramopoulos[2, 3], Stefan Engelhardt[2, 3], Markus H. Schwab[4, 11], Matthias Kneussel[5], Tim Czopka[1,6], Diane L. Sherman[7], Peter J. Brophy[7], Thomas Misgeld[1, 8, 9, 13*#], Monika S. Brill[1, 9, 13*]

[1] Institute of Neuronal Cell Biology, Technische Universität München, Biedersteiner Straße 29, 80802 Munich, Germany.

[2] Institute of Pharmacology and Toxicology. Technische Universität München, 80802 Munich, Germany;

[3] German Center for Cardiovascular Research (DZHK), partner site Munich Heart Alliance, 80802 Munich, Germany

[4] Department of Cellular Neurophysiology, Hannover Medical School, 30625 Hannover, Germany

[5] University Medical Center Hamburg-Eppendorf, Center for Molecular Neurobiology (ZMNH), Institute for Molecular Neurogenetics, Falkenried 94, 20251 Hamburg, Germany

[6] Centre for Clinical Brain Sciences, University of Edinburgh, Edinburgh EH16 4SB, UK

[7] Centre for Discovery Brain Sciences, University of Edinburgh, Edinburgh EH16 4SB, UK

[8] German Center for Neurodegenerative Diseases (DZNE), Feodor-Lynen-Straße 17, 81377 Munich, Germany

[9] Munich Cluster of Systems Neurology (SyNergy), Feodor-Lynen-Straße 17, 81377 Munich, Germany

[10] Present address: École Polytechnique Fédérale de Lausanne, SB IPHYS LEB BSP 428 (Cubotron UNIL), Lausanne, Switzerland

[11] Present address: Guus Vleugelplantsoen 26, 3544HR Utrecht, The Netherlands

[12] Present address: Department of Neurogenetics, Max-Planck-Institute of Experimental Medicine, 37075 Goettingen, Germany

[13] These authors contributed equally

*Correspondence: monika.leischner-brill@tum.de (M.S.B.), thomas.misgeld@tum.de (T.M.)

#Lead contact

Running title: Myelination during axonal remodeling

Keywords: Myelin, nodes of Ranvier, plasticity, synapse elimination, neuromuscular junction, axon, Schwann cells, Caspr, Neuregulin

Characters: 27,365 (characters not including spaces, without methods and references)

Figures: 7 (+ 4 Suppl. Figures)

SUMMARY

Postnatal motor neurons undergo extensive competitive remodeling and synchronously myelinate. Wang et al. now reveal that axon remodeling and myelination intersect: While myelination does not predetermine competition outcome, completing remodeling allows myelination to accelerate. This involves cytoskeletal maturation, which enables increased delivery of pro-myelinating signals.

ABSTRACT

Neuronal remodeling and myelination are two fundamental processes during neurodevelopment. How they influence each other remains largely unknown, even though their coordinated execution is critical for circuit function and often disrupted in neuropsychiatric disorders. It is unclear, whether myelination stabilizes axon branches during remodeling or whether ongoing remodeling delays myelination. By modulating synaptic transmission, cytoskeletal dynamics and axonal transport in mouse motor axons, we show that local axon remodeling delays myelination onset and node formation. Conversely, glial differentiation does not determine outcome of axon remodeling. Delayed myelination is not due to a limited supply of structural components of the axon-glial unit, but rather triggered by increased transport of signaling factors that initiate myelination, such as neuregulin. Further, transport of pro-myelinating signals is regulated via local cytoskeletal maturation related to activity-dependent competition. Our study reveals an axon branch-specific fine-tuning mechanism that locally coordinates axon remodeling and myelination.

INTRODUCTION

Myelin enables saltatory conduction and provides trophic support to the sheathed axons (Huxley and Stämpeli, 1949; Vabnick and Shrager, 1998; Yin et al., 2006; Simons and Trotter, 2007; Nave, 2010). In

addition, recent observations in the central nervous system (CNS) indicate that myelin contributes to fine-tuning of neural circuits (Fields, 2015; Chang et al., 2016; Kaller et al., 2017). For instance, myelin sheaths and nodes of Ranvier — ion channel-enriched axon segments interspersed between myelin sheaths — show activity-dependent plasticity (Huff et al., 2011; Gibson et al., 2014; Mensch et al., 2015; Etxeberria et al., 2016; Korrell et al., 2019; Bacmeister et al., 2020) that *e.g.* appear to shape 'patchy' myelination patterns in neocortex (Tomassy et al., 2014). While activity-regulated myelination is less studied in the peripheral nervous system (PNS, Stevens and Fields, 2000; Fields, 2015), in the PNS, the axon-glial unit is more accessible than in the CNS, and the signaling pathways governing peripheral myelination are better understood (Taveggia et al., 2010; Pereira et al., 2012; Grigoryan and Birchmeier, 2015) . Thus, PNS development offers a privileged window into the intersection of axonal remodeling and myelin plasticity.

To capitalize on these advantages, we turned to a major site of PNS remodeling, the neuromuscular junction (NMJ). At mouse NMJs, axonal remodeling follows a predictable course during the first two postnatal weeks and can be followed at the single axon branch level (Lichtman and Sanes, 2003; Walsh and Lichtman, 2003). At birth, multiple motor axon branches innervate the same postsynaptic site (Tapia et al., 2012). Subsequently all but one of these presynaptic inputs are eliminated by a two-step process that first involves activity-driven competition and then axon branch removal by cytoskeletal degradation (Buffelli et al., 2003; Brill et al., 2016), until lifelong innervation by a single axon is established (Tapia and Lichtman, 2012). Already during embryonic development, Schwann cells (SCs)—the glia of the PNS—surround growing motor axons and accompany them to the target muscle (Jessen and Mirsky, 2005). SCs initiate myelination perinatally, after SCs have been sorted to sheath individual axon branches (Jessen and Mirsky, 2005; Monk et al., 2015; Rasband and Peles, 2016). Overall, myelination follows a proximal-to-distal gradient along motor axons with myelination of terminal branches occurring last and asynchronously (Hildebrand et al., 1994; Yamamoto et al., 1996). This temporal correlation between axon-glial differentiation and cessation of developmental axon plasticity is a general feature across the nervous

system, and in the CNS can e.g. be observed in visual cortex (Luo and O'Leary, 2005; McGee et al., 2005; Simons and Trotter, 2007). In the PNS, myelination onset is determined by the level of Neuregulin-1 (Nrg1) type III on the axonal surface. Nrg1 binds to glial ErbB2/3 receptors on SCs, leading to phosphorylation of down-stream effectors, such as ERK1/2 and AKT (Garratt et al., 2000; Michailov et al., 2004; Taveggia et al., 2005; Iwakura and Nawa, 2013; Basak et al., 2015). While Nrg1 signaling is known to affect synapse development, the underlying signaling takes place at the NMJ itself, involving 'terminal' non-myelinating SCs, rather than myelinating SCs along the axon (Loeb, 2003; Hayworth et al., 2006; Lee et al., 2016). Thus, whether the timing of branch-specific myelination also depends on local availability of Nrg1, and whether Nrg1 signaling is locally regulated to coordinate axon remodeling and myelination remains to be elucidated. Hence, using the NMJ as a model, we asked: How are axonal competition and axon-glial differentiation coordinated at the single-branch level, and what is the signaling mechanism involved?

RESULTS

Axon-glial differentiation is delayed on branches engaged in remodeling

To study the intersection of axon remodeling and myelination, we took advantage of a thoracic nerve-muscle explant, including the *triangularis sterni* muscle, which is uniquely suited to study the cell biological dynamics of single axon branches (Kerschensteiner et al., 2008; Brill et al., 2013; Fig. 1 A). During the second postnatal week, most NMJs transition from double to single innervation (abbreviated in the figures as 'din' and 'sin', respectively), while myelin and nodes of Ranvier appear on terminal branches (Fig. 1 B). On three postnatal days (P7, 9 and 11), we quantified the number of NMJs still engaged in synaptic competition using *triangularis sterni* muscles derived from *Thy1*-XFP mice, where motor axons are fluorescently labeled (Feng et al., 2000; Fig. 1, C and D). In parallel, we determined the state of axon-glial differentiation on singly innervating terminal branches based on the presence of immunostained Caspr1 (contactin-associated protein 1; Rasband and Peles, 2016) accumulations along a given terminal branch.

We did not distinguish further between fully formed nodes (paranodes on both sides) and partially formed heminodes, resulting in a binary score (Caspr+ *vs.* Caspr- terminal branches; Fig. 1, C and D). We observed a concomitant resolution of synaptic competition (*i.e.* decreasing percentage of doubly innervated synapses) and increasing paranodal formation on 'winner' branches (Fig. 1 D). Finally at P13, all NMJs established single innervation (100 ± 0%, *n* = 3 mice, 100 NMJs per animal) and all terminal branches started to form paranodes (100 ± 0%, *n* = 3 mice, 30 NMJs per animal). Next, we immunostained for myelin and other nodal components in *Thy1*-XFP mice at P9. In parallel to Caspr, nodal (voltage-gated sodium channel, Nav), juxta-paranodal (contactin-2, CNTN2), and internodal (myelin protein zero, MPZ) markers emerged on terminal branches (Fig. 1, E and F; Doyle and Colman, 1993). Thus, as myelin and nodal compartments co-assemble rapidly (Girault and Peles, 2002; Schafer et al., 2006), we used Caspr immunostaining as a surrogate for overall axon-glial differentiation. Notably, when we focused on the branches still engaged in competition, we found significantly fewer branches immuno-positive for emerging nodal structures, resulting in an overall delay of axon-glial differentiation of roughly two days (~33% of the full 6-day myelination period) compared to their winner siblings. This finding was consistent across all markers tested (Fig. 1 F). Thus, ongoing competition, and hence sustained plasticity, of terminal axon branches coincides with a transient stall of myelination and node formation. We considered two explanations for this delay: (1) Slower assembly of structural components of the axon-glial unit, or (2) reduced pro-myelinating signals. To disambiguate these scenarios, we analyzed the dynamics of node formation during axonal remodeling.

Axon remodeling delays initiation, not progress of axon-glial differentiation

To measure the progress of axon remodeling, as well as the onset of node formation on individual motor axon branches, we characterized transgenic mice expressing GFP-tagged Caspr (Caspr-GFP; Fig. S1; Brivio et al., 2017) and generated mice expressing the β1 subunit of the voltage-gated sodium channel

93 tagged with GFP (β1-Nav-GFP; Fig. S1), both under control of the *Thy1* promotor. In both lines, progress of
94 synapse elimination and onset of node formation were unchanged compared to wild-type littermates at
95 P9 (Fig. S1 legend). We assessed the paranodal/nodal protein dynamics by fluorescence recovery after
96 photobleaching (FRAP, see Methods), and related the recovery rate to axonal competition status in β1-
97 Nav- or Caspr-GFP crossed to *Thy1*-OFP3 mice (Brill et al., 2011). GFP-positive clusters forming heminodes
98 were photo-bleached to approximately one third of their original fluorescence intensity (33 ± 3%, n = 135
99 nodes in 46 mice) and visualized again three hours later. The recovery was normalized to non-bleached
100 control nodes in the same field of view to account for imaging-related fluorescence loss (Fig. 2, A and C).
101 Surprisingly, at P9-11 we found significantly higher recovery rates of β1-Nav- or Caspr-GFP on competing
102 doubly innervating branches compared to singly innervating ones (Fig. 2, B and D) — suggesting that once
103 initiated, node formation progressed swiftly. We also found an age dependent decline (Rios et al., 2000):
104 Recently established nodal structures recover much faster than mature ones ('sin' P9-11 *vs.* 'sin' 6wk;
105 Caspr-GFP ~4.3 fold; β1-Nav-GFP ~4.4 fold; Zhang et al., 2012). At the same time, P9-11 nodes in proximal
106 positions ('stem'; Fig. 2, B and D) resembled distal mature (i.e. 6wk) nodes, consistent with the known
107 myelination gradient (Hildebrand et al., 1994). Hence, our data favor a mechanism where axonal
108 competition delays initiation, but not progress of axon-glial maturation. However, myelination and node
109 formation are still initiated on a subset of competing, doubly innervating axon branches (*cf.* Fig. 1 F). Thus
110 we wondered, whether disparate progress of axon-glial maturation influences the competition outcome.

111 **Axon-glial maturation does not convey an advantage in synaptic competition**

112 To address the effect of a branch's axon-glial maturation status on competition, we related initiation of
113 node formation to synaptic territory (*i.e.* the fraction of an NMJ that a terminal branch innervates).
114 Synaptic territory is a well-established indicator of probable competition outcome (Gan and Lichtman,
115 1998; Walsh and Lichtman, 2003; Brill et al., 2016). We determined synaptic territory using the 'Brainbow'

approach to individually color motor units (*ChAT*-Cre x *Thy1*-Brainbow-1.1; Fig. 3 A; Livet et al., 2007; Rossi et al., 2011) and immunostained for Caspr to reveal node formation along terminal branches at P9. Throughout all stages of axonal competition (1-99% territory), less than ~20% of the branches were Caspr-positive, and there was no correlation of myelination onset to synaptic territory (Fig. 3 B). However, once competition was resolved, Caspr was present on ~50% of the singly innervating terminal branches (100% territory; $\chi 2$ test, 1-99% *vs.* 100%, $p < 0.0001$, $n = 749$ axon branches in 45 mice; Fig. 3 B), suggesting a swift lift of the brake on axon-glial differentiation once competition was resolved. This lack of correlation contrasts with other cell biological features of terminal branches, *e.g.* cytoskeletal stability, organelle transport or caliber, which are highly correlated to synaptic territory (Keller-Peck et al., 2001; Brill et al., 2016). Moreover, the measured distribution of node formation patterns on competing axons, *e.g.* the fraction of NMJs where node formation had started on the winning (51-99% territory), the losing (1 – 49% territory), or neither of the competing branches, matched a random binomial distribution (14% 'din' myelinated across 1-99% territory, $n = 520$ 'din' NMJs in 35 mice; Fig. 3 C). This, however, does not rule out caliber as a central driver of node formation onset, as known for other PNS settings, where 1 µm represents a critical threshold for myelination (Voyvodic, 1989; Peters et al., 1991). Therefore we analyzed the diameter of competing branches with or without emerging nodes (Fig. 3 D), and found no difference between the groups during all stages of competition. We even found—albeit rarely—partially myelinated axon branches that lost against a non-myelinated competitor (Fig. 3, F and G). Only in retreating branches were the pruning axons with emerging nodes significantly thicker than their unmyelinated counterparts (Fig. 3 D), possibly due to the protective effect of myelin on axonal structures, as axon stretches covered by MPZ are significantly thicker than MPZ negative stretches along the same retreating branches (Fig. 3 E; Nave, 2010). Hence, axon-glial differentiation neither decides competition, nor prohibits axon pruning (*cf.* McGee et al., 2005). Together, the data suggest a unidirectional relationship, with ongoing axon remodeling delaying axon-glial maturation, but not the converse. Next, we wanted to test which phase of

synapse remodeling impacted axon-glial maturation to narrow down possible underlying signaling mechanisms.

Suspending competition, but not late branch removal, delays axon branch myelination

Synapse remodeling can be divided into several phases (Kano and Hashimoto, 2009; Turney and Lichtman, 2012), with an early activity-dependent competition phase driven by neurotransmission (Buffelli et al., 2003), followed by a late execution phase involving cytoskeletal break-down and glial engulfment (Bishop et al., 2004; Brill et al., 2016). First, we intervened during competition by irreversibly blocking postsynaptic acetylcholine receptors (AChRs) using unilateral thoracic injection of α-bungarotoxin (BTX, Akaaboune et al., 1999; Kummer et al., 2004) of P7 *Thy1*-XFP mice (Fig. 4 A). Paired analysis on contra- *vs.* ipsilateral *triangularis sterni* muscles two days later (P9; Fig. 4, B and C) revealed that more multiple innervation was maintained after BTX injection (Fig. 4 D; Loeb et al., 2002; Buffelli et al., 2003). Notably, the number of Caspr-positive winner branches ('sin') was significantly reduced (Fig. 4 E), suggesting that blocking neurotransmission delays the initiation of node formation. At the same time, we neither measured a change of axonal SC number, nor of internode or terminal branch length after BTX treatment (Fig. S2, A–D). Under physiological condition, the number of SCs slightly increases as competition resolves (indicated by reduced SC length; Fig. S2, E and F). We therefore hypothesized that BTX injection maintained terminal branches in a more juvenile state. Thus, we turned to the microtubular cytoskeleton as an important indicator for axonal maturation, since microtubular mass increases as the branch gains synaptic territory (Brill et al., 2016). The initiation of myelination correlates with an increase in tubulin content (Fig. S2 G and H). Following BTX injection, microtubular mass on winner axons ('sin') decreased to ~60%, while competing axons ('din') were not affected (Fig. 4, F and G). This hints at the possibility that the delayed node formation following transmission block is due to reduced microtubular mass.

To manipulate axonal microtubules, we genetically deleted spastin, a microtubule-severing enzyme (spastin KO), where we confirmed a delay in axon branch removal (Fig. 4, H–J; Brill et al., 2016). Indeed, loss of spastin led to accelerated node formation in competing axons ('din') compared to wild-type (WT; Fig. 4 K). That this represented a cell autonomous effect in motor neurons was corroborated by inducing subset deletion in conditional spastin$^{fl/fl}$ x TdTomato reporter mice (Brill et al., 2016) using a cre-encoding adeno-associated virus (AAV9-*CMV*-iCre; Fig. S3). While we again found delayed axon remodeling (Brill et al., 2016), node formation was now accelerated on competing branches (Fig. S3 C), where TdTomato expression indicated spastin deletion. Overall, microtubular mass was increased in spastin-deleted terminal axon branches (Fig. 4, L and M; Brill et al., 2016), while axonal caliber was unaffected (Fig. S3 D), contrasting the increase in nodal formation specifically on competing branches. This suggests that the microtubular cytoskeleton is the limiting factor to initiate node formation in competing branches, but not on winner axons, perhaps arguing for a two-component system, where each can be limiting in different stages. Moreover, the divergent axon-glial differentiation outcomes of postsynaptic block vs. spastin deletion, which both delay remodeling, points to a mechanism that is blocked by ongoing activity-dependent competition, but can be overcome by increasing microtubular mass. As the microtubular cytoskeleton sustains axonal transport (which requires tracks and cargoes), we next tested if reducing anterograde transport would affect local initiation of axon-glial differentiation.

Local axonal transport regulates terminal branch myelination during remodeling

To reduce transport in motor neurons, we overexpressed the cargo-binding domain (CBD) of kinesin-1 heavy chain (KHC), a key molecular motor driving anterograde transport (Hirokawa et al., 2009). This results in a dominant-negative mutant (KHC-CBD), which still binds cargoes, but lacks the motor domain and competes with endogenous kinesin-1, thus impairing transport of organelles and nodal components *in vitro* (Cai et al., 2005; Barry et al., 2014). To test the efficacy of this approach *in vivo*, we turned to

zebrafish as an easily accessible model for assaying effects of myelination-regulating signals (Czopka and Lyons, 2011). We used the Gal4/UAS system to transiently co-express *UAS*-GFP-KHC-CDB and *UAS*-mitoTagRFP-T in Rohon Beard sensory neurons, in which mitochondrial transport can be easily monitored (Plucińska et al., 2012). KHC-CBD overexpression in this system substantially reduced mitochondrial transport per minute (reduction from 0.61 ± 0.11 in control to 0.10 ± 0.02 in anterograde and 0.28 ± 0.04 to 0.10 ± 0.04 in retrograde direction at 2 days post fertilization, dpf; $P < 0.01$, Mann-Whitney test, $n \geq 4$ zebrafish per group, ≥ 4 axons). We then analyzed spinal motor neurons, which start to be myelinated at 3 dpf in zebrafish (D'Rozario et al., 2017). To down-regulate axonal transport while monitoring myelination progress, we expressed GFP-KHC-CBD or GFP alone under the neuronal *cntn1b* promoter in Tg(mbp:RFP) zebrafish, where all compacted internodes are fluorescently labelled by a membrane-targeted RFP (Auer et al., 2018; Fig. S4, A–E). On 6 dpf, axon length in Tg(mbp:RFP) zebrafish injected with cntn1b-GFP-KHC-CBD was similar to controls (Fig. S4 F), but strikingly, the myelinated axon length was only half compared to controls (Fig. S4 G). This supports the notion that PNS myelination depends on axonal transport.

We next probed whether this was true in murine motor axons during remodeling. In *Thy1*-β1-Nav-GFP animals, emerging β1-Nav-GFP clusters correlate with higher anterograde particle transport in terminal branches (Fig. 5). Among all β1-Nav-GFP positive branches, winner axons ('sin') had the highest anterograde transport rate (Fig. 5 B). Together, this is in line with our previous observation that microtubular mass correlates with node formation (Fig. S2 H). We then injected an AAV9 encoding KHC-CBD and iCre under control of the neuronal human synapsin promoter (AAV9-*hSyn*-iCre-p2a-KHC-CBD) into neonatal mice (Fig. 5 A). In AAV injected *Thy1*-β1-Nav-GFP x TdTomato reporter mice, we found a significant reduction in β1-Nav-GFP anterograde transport, while retrograde was unaffected (Fig. 5 B). Notably, the onset of node formation was significantly delayed in reporter-positive branches compared to negative ones, which served as internal controls (Fig. 5, C and D). This points to a transport-delivered signal, which locally times the onset of axon-glial differentiation of terminal axon branches.

Local disparity of pro-myelinating factors in terminal branches correlates with competition status

Nrg1 type III is a candidate for a transported pro-myelination signal, as this signaling factor locally needs to reach a critical threshold to initiate axon-glial differentiation (Taveggia et al., 2005; Nave and Salzer, 2006; Birchmeier and Nave, 2008; Velanac et al., 2012) by activating downstream effectors in SCs such as ERK1/2 and AKT (Ogata et al., 2004; Taveggia et al., 2005; Basak et al., 2015; Duregotti et al., 2015). To investigate Nrg1 type III function during axon remodeling, we crossed floxed Nrg1 type III (Velanac et al., 2012) to TdTomato reporter mice and injected neonates with AAV9-*CMV*-iCre (Fig. S3 E). As expected, myelination was severely impaired in TdTomato-positive branches compared to internal control axons (Fig. S3, F–H). We further tested if increased Nrg1 type III levels are sufficient to remove the competition-dependent block on myelination employing *Thy1*-Nrg1 type III-HA mice, where Nrg1 type III is tagged with hemagglutinin (Fig. 6 A and B). Here axon remodeling was transiently accelerated (Lee et al., 2016), and overall nodes form significantly earlier (Fig. 6 C–F; Velanac et al., 2012). Notably the myelination delay on competing 'din' branches was preserved, most likely reflecting the endogenous distribution of Nrg1 type III (Fig. 6 F).

To analyze local distribution of Nrg1 type III with single axon precision, we immunostained for the HA-tag and visualized SCs and axons (Fig. 7, A and B). Strikingly, we detected a higher HA-signal along winner 'sin' branches compared to competing 'din' axons, in line with differential trafficking regulated by competition-regulated cytoskeletal maturation (Fig. 7 C). Corroborating differential Nrg1 signaling, we measured significantly higher levels of activated forms of both ERK1/2 (pERK) and AKT (pAKT) surrounding winner 'sin' axons (Fig. 7, D–G). As myelination initiation on winner branches was reduced following neurotransmission blockade, HA-tagged Nrg1 type III and pERK signals also significantly decreased in 'sin' branches (Fig. 7, H and I). Transgenic expression of Nrg1 type III did not change the density neither area of acetylcholine receptors (Fig. 7 J and K). Therefore, Nrg1 type III likely impacts myelination via its promyelinating effects rather than by modulating postsynaptic feedback (Velanac et al., 2012; Kamezaki

et al., 2016). Indeed, the only phenotype we observed at the endplate was a premature shape change of the acetylcholine receptor distribution in *Thy1*-Nrg1 type III-HA mice compared to wild-type littermates (Fig. 7 L; *cf*. Lee et al., 2016).

DISCUSSION

Taken together, our data suggest that during motor axon remodeling, a pro-myelination signal—such as Nrg1—paces branch myelination, which is locally limited by axonal transport and depends on local regulation of cytoskeletal integrity. Thus, axon-glial differentiation is delayed until competition resolves and the axonal cytoskeleton matures. Notably, according to this model, axon dismantling and myelination initiation both depend on mechanisms that regulate the microtubular cytoskeleton (Brill et al., 2016). This model also links anterograde transport to a signaling function, which previously was mostly considered for retrograde transport, *e.g*. delivering neurotrophic factors (Je et al., 2012; Yamashita, 2019).

The intersection of axon remodeling and myelination is widespread (Feinberg, 1982; Bernstein and Lichtman, 1999; Woo and Crowell, 2005; Barres, 2008) and might play a general role in the activity-dependent sculpting of efficient neuronal networks (Luo and O'Leary, 2005; Tapia and Lichtman, 2012; de Hoz and Simons, 2015; Chang et al., 2016). The prevailing notion has been that myelination might terminate axonal plasticity by 'cementing' axons in place, thus contributing to closing the critical remodeling period (Caroni and Schwab, 1988; McGee et al., 2005; Geoffroy and Zheng, 2014; Kalish et al., 2020). Indeed, we observed myelination initiation predominantly on winner axon branches ('sin'), *i.e.* after competition was resolved (Fig. 1). However, while determining the exact start and progression speed of myelination is technically challenging (thus we resorted to a 'binary' readout of Caspr+ vs. Caspr- branches), our observations clearly reveal that competition delayed myelination, but not *vice versa* (Fig. 3). A subset of competing axons still initiated myelination, but this did not convey a measurable advantage during competition, as no relationship between myelination and synaptic territory was apparent in our data. Even

some retreating axons were myelinated, including in cases where the likely competing branch was not (Fig. 3 G). Still, in general myelination was prevented on axon branches that were fated for removal. As myelin is an extremely stable structure (Simons and Trotter, 2007; Hughes et al., 2018), which might be metabolically 'expensive' to build (Nave and Trapp, 2008; Harris and Attwell, 2012) and requires a dedicated mechanism for dismantling, it seems economical to delay myelination until pruning is resolved (McGee et al., 2005; Cheng and Carr, 2007). Thus our results support a view where myelin might act as participant in, but not as the terminator of circuit plasticity (Mount and Monje, 2017; but *cf*. Roche et al., 2014).

How do competing axon branches delay myelination? A number of cell biological features of such branches scale with its synaptic territory during competition, *e.g.* cytoskeletal stability, organelle transport or axon caliber (Keller-Peck et al., 2001; Brill et al., 2016). We can rule out the hypothesis that axon caliber dictates myelination onset, since axon caliber did not differ between myelinated and unmyelinated competing branches (Fig. 3 D; Goebbels et al., 2010), even though we found evidence that along a given branch, myelination has an impact on local diameter (Fig. 3 E). To further probe the mechanism that times myelination onset, we manipulated activity-driven competition (Buffelli et al., 2003) using local BTX injections (Fig. 4). This intervention is muscle-specific, therefore less likely to affect axon-SC communication, compared to blocking axonal action potential conduction or acetylcholine release (Misgeld et al., 2002; Lorenzetto et al., 2009). Notably, while there exists some cholinergic axon-Schwann cell communication, this typically involves BTX-insensitive receptors (Rousse and Robitaille, 2006). In the past, chronic blockade of neuromuscular transmission, *e.g.* in chicken embryos treated with curare, has been shown to result in AChR cluster fragmentation and axonal sprouting (*cf*. Loeb et al., 2002; Loeb, 2003). Also, constitutive genetic ablation of choline acetyl transferase in motor axons leads to premature myelination in the phrenic nerve at birth (Misgeld et al., 2002). Still, these outcomes likely reflect the combination of presynaptic and sustained blockade, prone to elicit homeostatic compensation (Davis,

2013). Here, by using brief and local postsynaptic blockade, we found the expected delay in axon remodeling, but also a commensurate hiatus in myelination (Fig. 4, D and E). Thus, myelination onset appears to be part of the BTX-sensitive competition program, revealing an indirect role of neurotransmission in regulating the progress of PNS myelination (for the CNS, *cf.* Stevens et al., 2002; Gibson et al., 2014; Krasnow et al., 2018). Moreover, postsynaptic block induced a reduction in presynaptic microtubular mass on winner branches (Fig. 4 F and G), suggesting a silencing-induced delay in maturation, which chimes with a cytoskeletal mechanism of inducing myelination.

Indeed, in terminal axon branches, the microtubular cytoskeleton matures in parallel to an increase in synaptic territory (Brill et al., 2016). Accordingly, we observed that spastin deletion, which increased microtubular mass (Fig. 4, L and M), resulted in accelerated myelination specifically on competing branches, breaking the link between remodeling and myelination delay (Fig. 4 K). However, spastin deletion in winner branches did not affect the initiation of myelination. This suggests that the limiting factor in this setting could be cargo instead of track availability, as we reported previously for mitochondria (Marahori, 2020). Since microtubular content can locally regulate axonal transport (Kapitein and Hoogenraad, 2015; Roll-Mecak, 2019), hinting that myelination might depend on branch-specific transport. To test this, we expressed a dominant-negative kinesin mutant *in vivo*, which affects anterograde organelle delivery (Cai et al., 2005; Barry et al., 2014). In both zebrafish and mouse motor neurons this delayed myelination, despite the transport blockade being partial and short (Fig. 5 and Fig. S4). Taken together, our data suggest that in competing branches, transport of pro-myelinating cargos is restricted by an immature and increasingly severed microtubular cytoskeleton (Brill et al., 2016).

Since our FRAP experiments suggest that nodal components are not limited in competing branches (Fig. 2), we focused on Nrg1 type III as the putative factor determining myelination onset for the following reasons: Nrg1 signaling (1) is the master regulator of PNS myelination (Birchmeier and Nave, 2008; Grigoryan and Birchmeier, 2015); (2) acts in a threshold-based manner (Garratt et al., 2000; Michailov et

al., 2004; Taveggia et al., 2005; Nave and Salzer, 2006); (3) is steeply upregulated during the synapse remodeling period (Lee et al., 2016), while its axonal presence is limited (Velanac et al., 2012). Indeed, we demonstrated that HA-tagged Nrg1 accumulates faster on winner than on competing branches (Fig. 7 C), and down-stream pathways of Nrg1 signaling are preferentially activated in SCs around winner branches (Fig. 7, F and G). It would have further strengthened our argument if increased Nrg1 could be observed in spastin deleted axons. Likely due to chromosomal incompatibility of the Nrg1 transgene insertion site and the spastin locus, we tested the converse setting and showed that HA-tagged Nrg1 distribution and down-stream signaling decrease upon BTX blockade (Fig. 7, H and I). The fact that Nrg1 overexpression accelerates both myelination and synapse elimination (Fig. 6; Lee et al., 2016) further strengthens our conclusion that myelination *per se* does not terminate remodeling. However, it is technically challenging to disambiguate whether Nrg1 signals directly from the axonal surface to myelinating SCs, or through a more complicated feedback via muscle and/or terminal SCs. Yet we did not measure a difference in postsynaptic acetylcholine receptor density neither area between *Thy1*-Nrg1 type III-HA and wild-type littermates (Fig. 7), suggesting Nrg1 likely functions via its promyelinating effects, rather than modulating muscular depolarization.

In summary, our experiments reveal an intercellular signaling mechanism that regulates myelination on a branch-to-branch level in the developing PNS. The extent of branch-specific Nrg1 accumulation, and hence the strength of the pro-myelination signal, is regulated by the axonal cytoskeleton as a spatially-resolved signaling hub (Janke, 2014). A similar local regulation between neuronal remodeling and myelination can be relevant in many developing neural circuits, *e.g.* certain cortical axon types are myelinated in a highly local fashion (Tomassy et al., 2014; Micheva et al., 2016). Moreover, when disturbed, such signaling could contribute to the disrupted timing of developmental events characteristic of some neuropsychiatric disorders, where axonal transport, neuronal remodeling and myelination all show subtle defects (Coleman and Perry, 2002; Luo and O'Leary, 2005; Mei and Nave, 2014).

MATERIALS AND METHODS

Mouse lines and husbandry

In all experiments, mice from both sexes were included. Animals were housed in individually ventilated cages with food and water ad libitum. All animal experiments were performed in accordance with the regulations by the local authorities, e.g. Government of Upper Bavaria. Experimental animals were kept together with littermates.

Experimental mice and genotyping

For labeling axons we used *Thy1*-XFP mice, which express OFP (*Thy1*-OFP3; Brill et al., 2011), YFP (*Thy1*-YFP16; Feng et al., 2000), or membrane-RFP (*Thy1*-Brainbow-1.1 line M; Livet et al., 2007) under the control of the *Thy1*-promotor (Feng et al., 2000). For FRAP experiments and node visualization in living explants, we used *Thy1*-Caspr-GFP (Brivio et al., 2017) and *Thy1*-β1-Nav-GFP transgenic mice (generated for this study, see below) crossed to *Thy1*-XFP mice. Synaptic territory of competing axonal branches was defined in *Thy1*-Brainbow-1.1 line M mice crossed to Cre-expressing lines: *CAG*-CreERT (gift from Dr. J. Livet, Institut de la Vision, Paris, France) or *ChAT*-IRES-Cre (Jackson, #6410; Rossi et al., 2011), which leads to individual fluorescent color combinations of membrane-targeted RFP, YFP, and CFP. For the crossing involving *CAG*-CreERT, 20µl of 1.5 mg/ml tamoxifen was subcutaneously injected on postnatal day (P) 3 to induce expression. Delayed synapse elimination was analyzed in spastin knock-out (KO) mice (Brill et al., 2016) or spastin floxed ($^{fl/fl}$) mice bred to *ROSA-CAG*-TdTomato or YFP reporter mice (Jackson, #7914, #7903; Madisen et al., 2010) injected with AAV9-CMV-iCre (provided by Dr. Engelhardt; Brill et al., 2016). Effects of transport modulation on myelin and nodal development was observed in TdTomato reporter mice crossed to *Thy1*-β1-Nav-GFP or *ROSA-CAG*-YFP mice injected with AAV9-hSyn-iCre-p2a-KHC-CBD. Precocious myelination was investigated in *Thy1*-Nrg1 type III-HA mice ("HANI", Velanac et al., 2012). To

investigate delayed nodal development, we injected AAV9-CMV-iCre into conditional Neuregulin knock-out mice (Nrg1 type III$^{fl/fl}$; Velanac et al., 2012) crossbred with *ROSA-CAG*-TdTomato reporter. To visualize SCs, we used *Plp*-GFP transgenic mice (Mallon et al., 2002). All experiments on *ROSA-CAG*-TdTomato reporter mice were performed in homozygous animals.

Genomic DNA was extracted from tail biopsies using a one-step lysis (lysis buffer in mM: 67 Tris pH 8.8, 16.6 $(NH_4)_2SO_4$, 6.5 $MgCl_2$, 5 β-mercaptoethanol, 10% Triton and 50 µg/ml Proteinase K; incubation at 55°C for 5 hours, followed by inactivation step 5 min at 95°C). PCR was performed with GoTaq Green Master Mix (Promega, #M7121) following a standard protocol, then DNA was separated on a 1.5 - 2 % agarose gel. Genotyping primers and expected products are listed in Table S1.

Generation of Thy1-β1-Nav-GFP transgenic mice

Transgenic mice expressing the beta 1 subunit of the sodium channel (β1-Nav) fused to GFP at the C-terminus under the control of the *Thy1.2* promoter (Caroni, 1997) were generated by pronuclear injection. The β1-Nav-GFP cDNA (McEwen et al., 2009) was cloned into the blunted XhoI site of the pTSC21k vector (Lüthi et al., 1997), released using Not I (Zonta et al., 2011), and used for pronuclear injection (Sherman and Brophy, 2000).

FRAP experiments and Caspr-GFP trafficking in nerve-muscle explant

Nerve-muscle explants from the thorax including the *triangularis sterni* muscle were prepared from young (postnatal day 7 - 14) or adult mice (6 weeks; Kerschensteiner et al., 2008; Brill et al., 2011, 2016). The rib cage was isolated from euthanized animals, and the skin and pectoral muscles over the rib cage were removed. The diaphragm was cut and the thorax was released by cutting the ribs close to the vertebral column. The dissection was continued in oxygenated precooled Ringer's solution (in mM: 125 NaCl, 2.5 KCl, 1.25 NaH_2PO_4, 26 $NaHCO_3$, 2 $CaCl_2$, 1 $MgCl_2$, 20 glucose, oxygenated with 95 % O_2/ 5 % CO_2) in a 10 cm dish and remnants of muscles, thymus, pleura and lung were removed. The clean nerve-muscle

explant was pinned onto a Sylgard-coated 3.5 cm dish, superfused with oxygenated Ringer's solution, using shortened insect pins (0.25 mm Fine Science Tools, 26001-25), exposing the *triangularis sterni* muscle, the intercostal nerve and terminal motor neuron branches. During imaging the explant was kept at 31-33°C with a heating ring connected to an automatic temperature controller (TC-344C, Warner Instruments) and steadily perfused with Ringer's solution.

Trafficking measurements of β1-Nav-GFP particles in the terminal branches were performed with an Olympus BX51WI epifluorescence microscope equipped with ×20/0.5 N.A. and ×100/1.0 N.A. water-immersion objectives, an automated filter wheel (Lambda 10-3, Sutter Instrument), a CCD camera (CoolSnap HQ2, Visitron Systems), and a GFP ET filter set (AHF Analysentechnik). All devices were controlled by µManager 1.4 (Edelstein et al., 2014). Per movie, we acquired 200 images at 1 Hz using an exposure time of 500 ms. Total imaging time on explants was restricted to maximum two hours, except for in FRAP analysis (below).

For FRAP analysis, we used *Thy1*-Caspr-GFP and *Thy1*-β1-Nav-GFP mice and the same setup as described above for transport measurements. The laser (473 nm, DL-473, Rapp OptoElectronic) for photobleaching was manually focused on a labeled node of Ranvier (~5 μm^2) and the sample was bleached for 1 - 3 seconds. We performed FRAP on branches with heminodes during development, since fully developed nodes are rare at the investigated age. In adults, all measurements were performed on fully developed nodes. The GFP signal was imaged with 800 ms exposure time before and immediately after photobleaching with a GFP/mCherry dualband ET filter set (AHF Analysentechnik), then in one-hour intervals for three hours with 800 ms exposure time.

Mouse immunofluorescence and confocal microscopy

The thorax was fixed in 4 % paraformaldehyde (PFA) for one hour in 0.1 M phosphate buffer (PB) on ice and the *triangularis* muscle was dissected and extracted (Brill et al., 2011). For HA staining, the sample was

additionally treated for 1 h at 37°C in 5 % CHAPS. The fixed thorax was incubated overnight (or 72 h for HA, pERK and pAKT) at 4°C in the respective primary antibodies diluted in blocking solution (5 % BSA, 0.5 % Triton X-100 in 0.1 M PB). To label postsynaptic nicotinic acetylcholine receptors Alexa 488-, Alexa 594-, Alexa 647- or biotin-conjugated to α-bungarotoxin (BTX; Invitrogen, B13422, B13423, B35450, B1196; 50 µg/ml, 1:50) was added to the primary antibody mixture. The following primary antibodies were used in this study: anti-βIII-tubulin conjugated to Alexa 488 (BioLegend, AB_2562669; mouse IgG2a, 1:200), Alexa 555 (BD Pharmingen, #560339; mouse monoclonal, 1:200), Alexa 647 (BioLegend, AB_2563609; mouse IgG2a, 1:200). For labeling of nodal components antibodies against Caspr (Abcam, AB_869934, polyclonal rabbit; 1 mg/ml 1:400), MPZ (Aves Labs combined chicken IgY, 200 µg/ml, 1:200), CNTN2 (R&D Systems, AB_2044647; polyclonal goat IgG, 1:200), pan Nav subunit α (Abgent, AG1392; polyclonal rabbit, 1.0 mg/ml, 1:400). HA was stained with anti HA-tag antibody (Cell Signaling, AB_1549585; rabbit, 1:50) and phosphorylated ERK1/2 was stained with anti-phospho-p44/42 MAPK (Cell Signaling, AB_331646; rabbit, 1:200). Here we used the tyramide signal amplification (TSA Cyanine 3 System, Perkin Elmer, AB_2572409). Muscles were washed in 0.1 M PB, incubated for one hour at room temperature with corresponding secondary antibodies coupled to Alexa 488, Alexa 594 or Alexa 647 (Invitrogen, rabbit: #A-11070, #A-11072, #A-21246, #A-32790; mouse: #A-11005; chicken: #A-11042; #A-21449; goat: #A-11058) and washed again in 0.1 M PB. Muscles were mounted in Vectashield (Vector Laboratories) or Fluoromont-G (Southern Biotech) and image stacks were recorded using a confocal microscope (Olympus FV1000) equipped with x20/0.8 N.A. and x60/1.42 N.A. oil-immersion objectives (Olympus).

Generation of recombinant DNA

In order to generate the pTREK1-*hSyn*-iCre-p2a-KHC-CBD construct for the AAV9-*hSyn*-iCre-p2a-KHC-CBD production, we used the Gibson Assembly Master Mix (NEB). We recombined fragments from pEGFP-C1-KHC-CBD (Cai et al., 2005), the dsCMV-iCre and the pAAV-*hSyn*-DIO-HA-hM3D(Gq)-IRES-mCitrine plasmid (addgene #50454) and the p2a sequence. The produced amplicon was ligated into the single-

stranded AAV backbone plasmid pTREK1. The following oligonucleotides were used: AGTACTTAATACGACTCACTATAGGATGGTGCCCAAGAAG, TCCACGTCGCCGGCCTGCTTCAGCAGGGAGAAGT-TGGTGGCGTCCCCATCCTCGA, TGCTGAAGCAGGCCGGCGACGTGGAGGAGAACCCCGGCCCCAGTGCTGAGATT-GATTCT, and ATCATGTCTGGATCCTCGATAGTTTAAACTTACACTTGTTTGCCTC.

For zebrafish injections, we generated pDestTol2CG2_UAS:GFP-KHC-CBD-polyA and pTol2_cntn1b:KHC-CBD-GFP vectors using the Gateway system (Thermo Fisher). To produce the middle entry clone pME_GFP-KHC-CBD, the GFP-KHC-CBD sequence was amplified from the template plasmid (Cai et al., 2005). The PCR product was then recombined into the vector pDONR221 using BP clonase (Thermo Fisher). The final expression constructs pTol2_UAS:GFP-KHC-CBD and pTol2_cntn1b:GFP-KHC-CBD were then generated in multisite LR recombination reactions with the entry clones, p5E_UAS, p5E_cntn1b, pME_GFP-KHC-CBD, p3E_pA and pDestTol2_pA of the Tol2Kit (Kwan et al., 2007).

Generation of AAV9 (adeno-associated virus serotype 9)

HEK293-T cells were grown in 10-tray Cell Factories (Thermo Scientific) using Dulbecco's modified essential medium (Gibco) with 10 % fetal bovine serum (Gibco) and 1 % penicillin/streptomycin (Gibco). The cells were split into the Cell Factories 24 h prior to transfection to reach 80 % confluence at the time of transfection. Then, 420 µg of the pTREK1-*hSyn*-iCre-p2a-KHC-CBD plasmid and 1.5 mg of the helper plasmid (pDP9rs, kindly provided by Roger Hajjar) were introduced into the HEK293-T cells using polyethylenimine (Polysciences). Three days later the cells were harvested, lysed, benzonase-treated and the virus was isolated by ultracentrifugation through an iodixanol density gradient (Optiprep, Progen). Ringer lactate buffer (Braun) was used to replace iodixanol with the help of Vivaspin 20 columns, MWCO 100000 PES (Sartorius). Two 10-tray Cell Factories were pooled and concentrated to a total volume of 500 µl. AAV9 titers were determined by real-time PCR using SYBR Green Master Mix (Roche). Titers in the range of $1x10^{14}$ viral genome copies per milliliter (vg/ml) were acquired.

Neonatal AAV9 or α-BTX-injection

AAV9 was injected into neonatal pups according to previously published protocol (Passini and Wolfe, 2001). In short, P3 pups were anaesthetized with isoflurane (Abbott) and injected with 3 µl AAV9-CMV-iCre or AAV9-hSyn-iCre-p2A-KHC particles into the right lateral ventricle at a rate of 30 nl/s using a fine glass pipette (3.5" Drummond #3-000-203-G/X) attached to a nanoliter injector (Micro4 MicroSyringe Pump Controller connected with Nanoliter 2000, World Precision Instruments). All surgeries were conducted under ultrasound guidance (Vevo1100 Imaging System, with a Microscan MS550D transducer, Visualsonics). 0.05 % (wt/vol) trypan blue was added to the viral solution for visualizing the filling of the injected ventricles. Only whole litters were injected, and pups were allowed to recover on a heating mat before the litter was returned to their mother into the home cage and sacrificed on P9 for immunohistochemistry. To monitor Cre-mediated recombination, mice carried in addition to the respective genes (spastin or Nrg1 type III conditional knock-out), two TdTomato or YFP reporter alleles (homozygous), which resulted in robust expression of the reporter in a subset of motor neurons.

Injection of α-BTX on P 7 was administered in a similar manner, only the needle was inserted laterally under the skin of the right thorax, and 1 µl of a 50 mg/µl Alexa 488- or 594-conjugated BTX solution (Invitrogen, B13422, B13423) was injected. The contralateral (left) *triangularis sterni* muscle was unaffected and used as control. The injected pups were viable and active after the treatment, and not distinguishable from untreated controls. Ipsi- and contralateral *triangularis sterni* muscle were then *post hoc* stained with Alexa 594- or 488-conjugated BTX respectively, resulting in complementing stainings for blocked and unblocked AChRs. We confirmed a substantial degree of persisting blockade at P9 (11.9 ± 4.5 fold change of BTX staining on injected vs. non-injected side, $n \geq 50$ NMJs in 5 mice) and the absence of denervation (> 100 NMJs per mouse, n = 3 mice).

Zebrafish injection, immunostaining and confocal imaging

Fertilized Tg(mbp:RFP) eggs (Auer et al., 2018) at the one cell stage were pressure microinjected with 1 nl solution containing 20 - 40 ng/µl plasmid DNA (*cntn1b*:GFP-KHC-CBD or control *cntn1b:GFP*; Auer et al., 2018) and 25 - 50 ng/µl transposase mRNA. For immunohistochemistry, larval zebrafish at 6 dpf were euthanized with 4 mg/ml MS-222 (PHARMAQ) and then fixed overnight in 4 % PFA in 0.1 M PB. After fixation, the samples were washed three times in PBS, 0.1 % Tween20 and then immersed for 2 hours at room temperature in blocking solution (5 % BSA, 0.5 % Triton X-100 in 0.1 M PB), then incubated in primary antibody against α-tubulin (Sigma-Aldrich, #00020911, mouse, 1:200) at 4° C for 48 hours in blocking solution. Samples were washed and incubated in secondary antibody conjugated to Alexa 647 (Invitrogen, goat-anti-mouse #A-28181) overnight at 4°C (Hunter et al., 2011). Samples were washed again and embedded in Vectashield (Vector Laboratories). Image stacks were recorded using a confocal microscope (Olympus FV1000) equipped with a x20/0.8 N.A. oil-immersion objective.

To label Rohon-Beard neurons, fertilized embryos from wild-type fish were co-injected with a sensory neuron-specific Gal4 driver construct (containing enhancer elements from *isl1*; Sagasti et al., 2005) together with UAS:KHC-CBD-GFP and UAS:mitoTagRFP-T plasmids (each at 5 ng/ul). Alternatively, UAS:KHC-CBD-GFP and UAS:mitoTagRFP-T plasmids were co-injected into fertilized eggs from the *isl2b*:Gal4 line (Fredj et al., 2010). At 2 dpf, embryos were anesthetized using 0.2 mg/ml MS-222 (PHARMAQ) and embedded in UltraPure Low Melting Point Agarose (Thermo Fisher) on a glass coverslip. After selecting double labeled Rohon-Beard neurons, mitochondrial transport was imaged for at least 50 min in the stem axon using the wide-field microscope configured as in the FRAP experiments. We acquired movies with an imaging frequency of 2 Hz and an exposure time between 200 and 500 ms for each fish (Plucińska et al., 2012).

Image processing/representation and quantification

Innervation patterns was determined by counting the number of innervating terminal branches ending on each BTX stained neuromuscular junction (NMJ) in ImageJ/Fiji (Schindelin et al., 2012). The myelination status of a terminal branch (axon from last bifurcation until NMJ) was determined by any presence of clustered markers of nodal or internodal differentiation (Caspr, CNTN2, MPZ, Nav). Immunostaining on branchpoints were excluded due to difficulties to discern from the more prominent nodal structures on the stem axon. Axon diameter was determined by measuring the area of the entire terminal branch, then divided by the length of the branch, resulting in an averaged axon diameter. We verified the precision of our axonal diameter measurement by comparison with other methods to determine axonal diameter (*e.g.* averaged multi-site measurements; determination of smallest diameter *etc.*), and found no significant difference between Caspr-positive and negative axons in measured caliber with the different approaches we tested.

Tubulin content of axons was determined by manually placing regions of interest in a single optical section within an axon, and the mean grey values were averaged for each channel. We have previously established that immunohistochemically determined tubulin content correlates linearly with microtubule density as measured by electron microscopy, once corrected for an offset likely representing non-polymerized tubulin (Brill et al., 2016).

For FRAP analysis, in focus images were manually aligned and the intensity of the bleached area was measured with the polygon tool. The background intensity was measured in a dark and even area, and another GFP-positive paranode in the same field of view was used as control to correct for the recovery rate.

For zebrafish myelination, the motor axon length was determined using the segmented line tool based on α-tubulin staining, and the length of the myelinated stretch is likewise determined based on mbp:RFP fluorescence.

Colocalization of GFP-positive Nav puncta and antibody staining was analyzed in single optical sections of unprocessed images.

To determine transport rates of mitochondria or β1-Nav-GFP particles travelling along the axons, we counted the number of fluorescent particles passing through a region in focus of the axon quantified.

For image representation, maximum intensity projections were generated from confocal image stacks with ImageJ/Fiji, then further processed in Adobe Photoshop where channels were adjusted individually. For better visibility of dim structures gamma was adjusted in images that only represent morphological detail; no gamma adjustment was performed in quantitative images (all panels in Fig. 2, A and C; Fig. 4, F and L; Fig 6, A and B; Fig. 7, B and E; Fig. S2, G).

All analysis was performed with the experimenter blinded to the treatment or genotypes during imaging and scoring.

Statistical Analysis

Statistical tests were performed using the GraphPad PRISM software. Statistical significance was determined using the Mann-Whitney test (non-parametric test for two groups), following the Kruskal-Wallis test with post hoc Dunn's multiple comparisons test (non-parametric test for three or more groups) respectively. Unpaired t-test was used when the data set passed the D'Agostino & Pearson normality test. The $\chi 2$ test was used for comparing expected frequencies between groups, and the p-value calculated from the test was shown. Group sizes were determined using experience values from prior studies (*e.g.* Brill et al., 2016; Plucińska et al., 2012). $P < 0.05$ was considered to be significant, and indicated by "*"; $P < 0.01$ by "**"; $P < 0.001$ by "***"; and $P < 0.0001$ by "****". Bar graphs show mean + standard error of the mean. Violin plots depict median and quartiles excluding the outliers, which were identified with Tukey's test (Fig. 2, B and D; Fig. 5, B; Fig. S2, H; Fig. S3, D).

SUPPLEMENTAL MATERIAL

Supplemental information includes 4 supplemental figures and one supplemental table.

AUTHOR CONTRIBUTIONS

Conceptualization, M.W., T.M. and M.S.B.; Investigation, M.W., T.K., G.P. and Y.X.; Methodology, D.L.S., P.J.B.; Resources, P.A., S.E., M.H.S., P.B., D.S., M.K. and T.C.; Writing –Original Draft, M.W. and M.S.B.; Writing –Review & Editing, all authors; Supervision, T.M. and M.S.B.; Funding Acquisition, T.M.

ACKNOWLEDGEMENTS

We would like to thank M. and N. Budak, K. Wullimann and Y. Hufnagel for excellent technical assistance. We thank Dr. L. Godinho for critically reading the manuscript. We are grateful to Dr. J. Livet for the generous gift of *CAG*-CreERT mice and Dr. J. Trimmer for the Caspr antibody. Work in T.M.'s lab is supported by the Deutsche Forschungsgemeinschaft (DFG; CIPSM EXC114, CRC870, FOR 2879, Mi 694/7-1 and 8-1, TRR274 - TRR 274/1 2020; ID 408885537, projects B03, C02), the European Research Council (FP/2007-2013; ERC Grant Agreement n. 616791), the Gemeinnützige Hertie Stiftung, the German-Israeli Foundation (I-1200-237.1/2012), the German Center for Neurodegenerative Diseases (DZNE) and Technische Universität München's (TUM) Institute for Advanced Studies. T.M. and M.S.B. were further funded by the DFG-funded Excellence Cluster SyNergy (EXC 2145 – ID 390857198). M.S.B. is recipient or a DFG research grant (LE 4610/1-1). M.W. received support from the TUM PhD program 'Medical Life Sciences and Technology'. D.L.S. and P.J.B. were supported by an award from the Wellcome Trust (Grant No. 107008). The authors declare no competing financial interests.

REFERENCES

Akaaboune, M., S.M. Culican, S.G. Turney, and J.W. Lichtman. 1999. Rapid and reversible effects of activity on acetylcholine receptor density at the neuromuscular junction in vivo. *Science*. 286:503–507. doi:10.1126/science.286.5439.503.

Auer, F., S. Vagionitis, and T. Czopka. 2018. Evidence for myelin sheath remodeling in the CNS revealed by in vivo imaging. *Curr. Biol.* 28:549-559.e3. doi:10.1016/j.cub.2018.01.017.

Bacmeister, C.M., H.J. Barr, C.R. McClain, M.A. Thornton, D. Nettles, C.G. Welle, and E.G. Hughes. 2020. Motor learning promotes remyelination via new and surviving oligodendrocytes. *Nat. Neurosci.* 23. doi:10.1038/s41593-020-0637-3.

Barres, B.A. 2008. The mystery and magic of glia: a perspective on their roles in health and disease. *Neuron*. 60:430–440. doi:10.1016/j.neuron.2008.10.013.

Barry, J., Y. Gu, P. Jukkola, B. O'Neill, H. Gu, P.J. Mohler, K.T. Rajamani, and C. Gu. 2014. Ankyrin-G directly binds to kinesin-1 to transport voltage-gated Na+ channels into axons. *Dev. Cell*. 28:117–131. doi:10.1016/j.devcel.2013.11.023.

Basak, S., D.J. Desai, E.H. Rho, R. Ramos, P. Maurel, and H.A. Kim. 2015. E-Cadherin enhances neuregulin signaling and promotes Schwann cell myelination. *Glia*. 63:1522–1536. doi:10.1002/glia.22822.

Bernstein, M., and J.W. Lichtman. 1999. Axonal atrophy: The retraction reaction. *Curr. Opin. Neurobiol.* 9:364–370. doi:10.1016/S0959-4388(99)80053-1.

Birchmeier, C., and K.A. Nave. 2008. Neuregulin-1, a key axonal signal that drives schwann cell growth and differentiation. *Glia*. 56:1491–1497. doi:10.1002/glia.20753.

Bishop, D.L., T. Misgeld, M.K. Walsh, W.B. Gan, and J.W. Lichtman. 2004. Axon branch removal at developing synapses by axosome shedding. *Neuron*. 44:651–661. doi:10.1016/j.neuron.2004.10.026.

Brill, M.S., T. Kleele, L. Ruschkies, M. Wang, N.A. Marahori, M.S. Reuter, T.J. Hausrat, E. Weigand, M. Fisher, A. Ahles, S. Engelhardt, D.L. Bishop, M. Kneussel, and T. Misgeld. 2016. Branch-specific microtubule destabilization mediates axon branch loss during neuromuscular synapse elimination. *Neuron*. 92:845–856. doi:10.1016/j.neuron.2016.09.049.

Brill, M.S., J.W. Lichtman, W. Thompson, Y. Zuo, and T. Misgeld. 2011. Spatial constraints dictate glial territories at murine neuromuscular junctions. *J. Cell Biol.* 195:293–305. doi:10.1083/jcb.201108005.

Brill, M.S., P. Marinković, and T. Misgeld. 2013. Sequential photo-bleaching to delineate single Schwann cells at the neuromuscular junction. *J. Vis. Exp.* 71:e4460. doi:10.3791/4460.

Brivio, V., C. Faivre-Sarrailh, E. Peles, D.L. Sherman, and P.J. Brophy. 2017. Assembly of CNS nodes of Ranvier in myelinated nerves is promoted by the axon cytoskeleton. *Curr. Biol.* 27:1068–1073. doi:10.1016/j.cub.2017.01.025.

Buffelli, M., R.W. Burgess, G. Feng, C.G. Lobe, J.W. Lichtman, and J.R. Sanes. 2003. Genetic evidence that relative synaptic efficacy biases the outcome of synaptic competition. *Nature*. 424:430–434. doi:10.1038/nature01836.1.

Cai, Q., C. Gerwin, and Z.H. Sheng. 2005. Syntabulin-mediated anterograde transport of mitochondria along neuronal processes. *J. Cell Biol.* 170:959–969. doi:10.1083/jcb.200506042.

Caroni, P. 1997. Overexpression of growth-associated proteins in the neurons of adult transgenic mice. *J. Neurosci. Methods*. 71:3–9. doi:10.1016/S0165-0270(96)00121-5.

Caroni, P., and M.E. Schwab. 1988. Antibody against myelin associated inhibitor of neurite growth

neutralizes nonpermissive substrate properties of CNS white matter. *Neuron*. 1:85–96. doi:10.1016/0896-6273(88)90212-7.

Chang, K.-J., S.A. Redmond, and J.R. Chan. 2016. Remodeling myelination: implications for mechanisms of neural plasticity. *Nat. Neurosci.* 19:190–197. doi:10.1038/nn.4200.

Cheng, S.M., and C.E. Carr. 2007. Functional delay of myelination of auditory delay lines in the nucleus laminaris of the barn owl. *Dev. Neurobiol.* 67:1957–1974. doi:10.1002/dneu.20541.

Coleman, M.P., and V.H. Perry. 2002. Axon pathology in neurological disease: A neglected therapeutic target. *Trends Neurosci.* 25:532–537. doi:10.1016/S0166-2236(02)02255-5.

Czopka, T., and D.A. Lyons. 2011. Dissecting mechanisms of myelinated axon formation using zebrafish. *In* Methods in Cell Biology. 25–62.

D'Rozario, M., K.R. Monk, and S.C. Petersen. 2017. Analysis of myelinated axon formation in zebrafish. *Methods Cell Biol.* 138:383–414. doi:10.1016/bs.mcb.2016.08.001.

Davis, G.W. 2013. Homeostatic signaling and the stabilization of neural function. *Neuron*. 80:718–728. doi:10.1016/j.neuron.2013.09.044.

Doyle, J.P., and D.R. Colman. 1993. Glial-neuron interactions and the regulation of myelin formation. *Curr. Opin. Cell Biol.* 5:779–785. doi:10.1016/0955-0674(93)90025-L.

Duregotti, E., S. Negro, M. Scorzeto, I. Zornetta, B.C. Dickinson, C.J. Chang, C. Montecucco, and M. Rigoni. 2015. Mitochondrial alarmins released by degenerating motor axon terminals activate perisynaptic Schwann cells. *Proc. Natl. Acad. Sci. U. S. A.* 112:E497-505. doi:10.1073/pnas.1417108112.

Edelstein, A.D., M.A. Tsuchida, N. Amodaj, H. Pinkard, R.D. Vale, and N. Stuurman. 2014. Advanced methods of microscope control using μManager software. *J. Biol. Methods*. 1:10. doi:10.14440/jbm.2014.36.

Etxeberria, A., K.C. Hokanson, D.Q. Dao, S.R. Mayoral, F. Mei, S.A. Redmond, E.M. Ullian, and J.R. Chan. 2016. Dynamic modulation of myelination in response to visual stimuli alters optic nerve conduction velocity. *J. Neurosci.* 36:6937–6948. doi:10.1523/JNEUROSCI.0908-16.2016.

Feinberg, I. 1982. Schizophrenia: Caused by a fault in programmed synaptic elimination during adolescence? *J. Psychiatr. Res.* 17:319–334. doi:10.1016/0022-3956(82)90038-3.

Feng, G., R.H. Mellor, M. Bernstein, C. Keller-Peck, Q.T. Nguyen, M. Wallace, J.M. Nerbonne, J.W. Lichtman, and J.R. Sanes. 2000. Imaging neuronal subsets in transgenic mice expressing multiple spectral variants of GFP. *Neuron*. 28:41–51. doi:10.1016/S0896-6273(00)00084-2.

Fields, R.D. 2015. A new mechanism of nervous system plasticity: activity-dependent myelination. *Nat. Rev. Neurosci.* 16:756–67. doi:10.1038/nrn4023.

Fredj, N. Ben, S. Hammond, H. Otsuna, C. Bin Chien, J. Burrone, and M.P. Meyer. 2010. Synaptic activity and activity-dependent competition regulates axon arbor maturation, growth arrest, and territory in the retinotectal projection. *J. Neurosci.* 30:10939–10951. doi:10.1523/JNEUROSCI.1556-10.2010.

Gan, W.B., and J.W. Lichtman. 1998. Synaptic segregation at the developing neuromuscular junction. *Science*. 282:1508–1511. doi:10.1126/science.282.5393.1508.

Garratt, A.N., O. Voiculescu, P. Topilko, P. Charnay, and C. Birchmeier. 2000. A dual role of erbB2 in myelination and in expansion of the Schwann cell precursor pool. *J. Cell Biol.* 148:1035–1046. doi:10.1083/jcb.148.5.1035.

Geoffroy, C.G., and B. Zheng. 2014. Myelin-associated inhibitors in axonal growth after CNS injury. *Curr. Opin. Neurobiol.* 27:31–38. doi:10.1016/j.conb.2014.02.012.

Gibson, E.M., D. Purger, C.W. Mount, A.K. Goldstein, G.L. Lin, L.S. Wood, I. Inema, S.E. Miller, G. Bieri, J.B. Zuchero, B.A. Barres, P.J. Woo, H. Vogel, and M. Monje. 2014. Neuronal activity promotes oligodendrogenesis and adaptive myelination in the mammalian brain. *Science*. 344:1252304. doi:10.1126/science.1252304.

Girault, J.A., and E. Peles. 2002. Development of nodes of Ranvier. *Curr. Opin. Neurobiol.* 12:476–485. doi:10.1016/S0959-4388(02)00370-7.

Goebbels, S., J.H. Oltrogge, R. Kemper, I. Heilmann, I. Bormuth, S. Wolfer, S.P. Wichert, W. Möbius, X. Liu, C. Lappe-Siefke, M.J. Rossner, M. Groszer, U. Suter, J. Frahm, S. Boretius, and K.A. Nave. 2010. Elevated phosphatidylinositol 3,4,5-trisphosphate in glia triggers cell-autonomous membrane wrapping and myelination. *J. Neurosci.* 30:8953–8964. doi:10.1523/JNEUROSCI.0219-10.2010.

Grigoryan, T., and W. Birchmeier. 2015. Molecular signaling mechanisms of axon-glia communication in the peripheral nervous system. *BioEssays*. 37:502–513. doi:10.1002/bies.201400172.

Harris, J.J., and D. Attwell. 2012. The energetics of CNS white matter. *J. Neurosci.* 32:356–371. doi:10.1523/JNEUROSCI.3430-11.2012.

Hayworth, C.R., S.E. Moody, L. a Chodosh, P. Krieg, M. Rimer, and W.J. Thompson. 2006. Induction of neuregulin signaling in mouse schwann cells in vivo mimics responses to denervation. *J. Neurosci.* 26:6873–6884. doi:10.1523/JNEUROSCI.1086-06.2006.

Hildebrand, C., C.M. Bowe, and I.N. Remahl. 1994. Myelination and myelin sheath remodelling in normal and pathological PNS nerve fibres. *Prog. Neurobiol.* 43:85–141. doi:10.1016/0301-0082(94)90010-8.

Hirokawa, N., Y. Noda, Y. Tanaka, and S. Niwa. 2009. Kinesin superfamily motor proteins and intracellular transport. *Nat. Rev. Mol. Cell Biol.* 10:682–696. doi:10.1038/nrm2774.

de Hoz, L., and M. Simons. 2015. The emerging functions of oligodendrocytes in regulating neuronal network behaviour. *BioEssays*. 37:60–69. doi:10.1002/bies.201400127.

Huff, T.B., Y. Shi, W. Sun, W. Wu, R. Shi, and J.X. Cheng. 2011. Real-time CARS imaging reveals a calpain-dependent pathway for paranodal myelin retraction during high-frequency stimulation. *PLoS One*. 6:e17176. doi:10.1371/journal.pone.0017176.

Hughes, E.G., J.L. Orthmann-Murphy, A.J. Langseth, and D.E. Bergles. 2018. Myelin remodeling through experience-dependent oligodendrogenesis in the adult somatosensory cortex. *Nat. Neurosci.* 21:696–706. doi:10.1038/s41593-018-0121-5.

Hunter, P.R., N. Nikolaou, B. Odermatt, P.R. Williams, U. Drescher, and M.P. Meyer. 2011. Localization of Cadm2a and Cadm3 proteins during development of the zebrafish nervous system. *J. Comp. Neurol.* 519:2252–2270. doi:10.1002/cne.22627.

Huxley, A.F., and R. Stämpeli. 1949. Evidence for saltatory conduction in peripheral myelinated nerve fibres. *J. Physiol.* 108:315–339. doi:10.1113/jphysiol.1949.sp004335.

Iwakura, Y., and H. Nawa. 2013. ErbB1-4-dependent EGF/neuregulin signals and their cross talk in the central nervous system: Pathological implications in schizophrenia and Parkinson's disease. *Front. Cell. Neurosci.* 1–35. doi:10.3389/fncel.2013.00004.

Janke, C. 2014. The tubulin code: Molecular components, readout mechanisms, functions. *J. Cell Biol.* 206:461–472. doi:10.1083/jcb.201406055.

Je, H.S., F. Yang, Y. Ji, G. Nagappan, B.L. Hempstead, and B. Lu. 2012. Role of pro-brain-derived neurotrophic factor (proBDNF) to mature BDNF conversion in activity-dependent competition at developing neuromuscular synapses. *Proc. Natl. Acad. Sci. U. S. A.* 109:15924–15929. doi:10.1073/pnas.1207767109.

678 Jessen, K.R., and R. Mirsky. 2005. The origin and development of glial cells in peripheral nerves. *Nat. Rev.*
679 *Neurosci.* 6:671–82. doi:10.1038/nrn1746.

680 Kalish, B.T., T.R. Barkat, E.E. Diel, E.J. Zhang, M.E. Greenberg, and T.K. Hensch. 2020. Single-nucleus RNA
681 sequencing of mouse auditory cortex reveals critical period triggers and brakes. *Proc. Natl. Acad. Sci.*
682 *U. S. A.* 117. doi:10.1073/pnas.1920433117.

683 Kaller, M.S., A. Lazari, C. Blanco-Duque, C. Sampaio-Baptista, and H. Johansen-Berg. 2017. Myelin plasticity
684 and behaviour — connecting the dots. *Curr. Opin. Neurobiol.* 47:86–92.
685 doi:10.1016/j.conb.2017.09.014.

686 Kamezaki, A., F. Sato, K. Aoki, K. Asakawa, K. Kawakami, F. Matsuzaki, and A. Sehara-Fujisawa. 2016.
687 Visualization of Neuregulin 1 ectodomain shedding reveals its local processing in vitro and in vivo. *Sci.*
688 *Rep.* 6:1–11. doi:10.1038/srep28873.

689 Kano, M., and K. Hashimoto. 2009. Synapse elimination in the central nervous system. *Curr. Opin.*
690 *Neurobiol.* 19:154–161. doi:10.1016/j.conb.2009.05.002.

691 Kapitein, L.C., and C.C. Hoogenraad. 2015. Building the Neuronal Microtubule Cytoskeleton. *Neuron*.
692 87:492–506. doi:10.1016/j.neuron.2015.05.046.

693 Keller-Peck, C.R., M.K. Walsh, W.B. Gan, G. Feng, J.R. Sanes, and J.W. Lichtman. 2001. Asynchronous
694 synapse elimination in neonatal motor units: Studies using GFP transgenic mice. *Neuron*. 31:381–394.
695 doi:10.1016/S0896-6273(01)00383-X.

696 Kerschensteiner, M., M.S. Reuter, J.W. Lichtman, and T. Misgeld. 2008. Ex vivo imaging of motor axon
697 dynamics in murine triangularis sterni explants. *Nat. Protoc.* 3:1645–1653.
698 doi:10.1038/nprot.2008.160.

699 Korrell, K. V., J. Disser, K. Parley, A. Vadisiute, M. Requena-Komuro, H. Fodder, C. Pollart, G. Knott, Z.
700 Molnár, and A. Hoerder-Suabedissen. 2019. Differential effect on myelination through abolition of
701 activity-dependent synaptic vesicle release or reduction of overall electrical activity of selected
702 cortical projections in the mouse. *J. Anat.* 235:452–467. doi:10.1111/joa.12974.

703 Krasnow, A.M., M.C. Ford, L.E. Valdivia, S.W. Wilson, and D. Attwell. 2018. Regulation of developing myelin
704 sheath elongation by oligodendrocyte calcium transients in vivo. *Nat. Neurosci.* 21:24–30.
705 doi:10.1038/s41593-017-0031-y.

706 Kummer, T.T., T. Misgeld, J.W. Lichtman, and J.R. Sanes. 2004. Nerve-independent formation of a
707 topologically complex postsynaptic apparatus. *J. Cell Biol.* 164. doi:10.1083/jcb.200401115.

708 Kwan, K.M., E. Fujimoto, C. Grabher, B.D. Mangum, M.E. Hardy, D.S. Campbell, J.M. Parant, H.J. Yost, J.P.
709 Kanki, and C. Bin Chien. 2007. The Tol2kit: A multisite gateway-based construction Kit for Tol2
710 transposon transgenesis constructs. *Dev. Dyn.* 236:3088–3099. doi:10.1002/dvdy.21343.

711 Lee, Y. il, Y. Li, M. Mikesh, I. Smith, K.-A. Nave, M.H. Schwab, and W.J. Thompson. 2016. Neuregulin1
712 displayed on motor axons regulates terminal Schwann cell-mediated synapse elimination at
713 developing neuromuscular junctions. *Proc. Natl. Acad. Sci.* 113:E479–E487.
714 doi:10.1073/pnas.1519156113.

715 Lichtman, J.W., and J.R. Sanes. 2003. Watching the neuromuscular junction. *J. Neurocytol.* 32.
716 doi:10.1023/B:NEUR.0000020622.58471.37.

717 Livet, J., T.A. Weissman, H. Kang, R.W. Draft, J. Lu, R.A. Bennis, J.R. Sanes, and J.W. Lichtman. 2007.
718 Transgenic strategies for combinatorial expression of fluorescent proteins in the nervous system.
719 *Nature*. 450:56–62. doi:10.1038/nature06293.

720 Loeb, J. a, A. Hmadcha, G.D. Fischbach, S.J. Land, and V.L. Zakarian. 2002. Neuregulin expression at

721 neuromuscular synapses is modulated by synaptic activity and neurotrophic factors. *J. Neurosci.*
722 22:2206–2214. doi:10.1523/jneurosci.22-06-02206.2002.

723 Loeb, J.A. 2003. Neuregulin: An activity-dependent synaptic modulator at the neuromuscular junction. *J.*
724 *Neurocytol.* 32:649–664. doi:10.1023/B:NEUR.0000020640.84708.35.

725 Lorenzetto, E., L. Caselli, G. Feng, W. Yuan, J.M. Nerbonne, J.R. Sanes, and M. Buffelli. 2009. Genetic
726 perturbation of postsynaptic activity regulates synapse elimination in developing cerebellum. *Proc.*
727 *Natl. Acad. Sci. U. S. A.* 106:16475–16480. doi:10.1073/pnas.0907298106.

728 Luo, L., and D.D.M. O'Leary. 2005. Axon Retraction and Degeneration in Development and Disease. *Annu.*
729 *Rev. Neurosci.* 28:127–156. doi:10.1146/annurev.neuro.28.061604.135632.

730 Lüthi, A., H. Van Der Putten, F.M. Botteri, I.M. Mansuy, M. Meins, U. Frey, G. Sansig, C. Portet, M. Schmutz,
731 M. Schröder, C. Nitsch, J.P. Laurent, and D. Monard. 1997. Endogenous serine protease inhibitor
732 modulates epileptic activity and hippocampal long-term potentiation. *J. Neurosci.* 17:4688–4699.
733 doi:10.1523/jneurosci.17-12-04688.1997.

734 Madisen, L., T.A. Zwingman, S.M. Sunkin, S.W. Oh, H.A. Zariwala, H. Gu, L.L. Ng, R.D. Palmiter, M.J.
735 Hawrylycz, A.R. Jones, E.S. Lein, and H. Zeng. 2010. A robust and high-throughput Cre reporting and
736 characterization system for the whole mouse brain. *Nat. Neurosci.* 13:133–140. doi:10.1038/nn.2467.

737 Mallon, B.S., H.E. Shick, G.J. Kidd, and W.B. Macklin. 2002. Proteolipid promoter activity distinguishes two
738 populations of NG2-positive cells throughout neonatal cortical development. *J. Neurosci.* 22:876–885.
739 doi:10.1523/jneurosci.22-03-00876.2002.

740 Marahori, N.A. 2020. Cytoskeletal rearrangement during developmental motor axon remodeling.
741 Technical University Munich. 98 pp.

742 McEwen, D.P., C. Chen, L.S. Meadows, L. Lopez-Santiago, and L.L. Isom. 2009. The voltage-gated Na+
743 channel β3 subunit does not mediate trans homophilic cell adhesion or associate with the cell
744 adhesion molecule contactin. *Neurosci. Lett.* 462:272–275. doi:10.1016/j.neulet.2009.07.020.

745 McGee, A.W., Y. Yang, Q.S. Fischer, N.W. Daw, and S.M. Strittmatter. 2005. Experience-driven plasticity of
746 visual cortex limited by myelin and Nogo receptor. *Science*. 309:2222–6.
747 doi:10.1126/science.1114362.

748 Mei, L., and K.A. Nave. 2014. Neuregulin-ERBB signaling in the nervous system and neuropsychiatric
749 diseases. *Neuron*. 83:27–49. doi:10.1016/j.neuron.2014.06.007.

750 Mensch, S., M. Baraban, R. Almeida, T. Czopka, J. Ausborn, A. El Manira, and D.A. Lyons. 2015. Synaptic
751 vesicle release regulates myelin sheath number of individual oligodendrocytes in vivo. *Nat. Neurosci.*
752 18:628–30. doi:10.1038/nn.3991.

753 Michailov, G. V., M.W. Sereda, B.G. Brinkmann, T.M.H. Fischer, B. Haug, C. Birchmeier, L. Role, C. Lai, M.H.
754 Schwab, and K.-A.A. Nave. 2004. Axonal Neuregulin-1 Regulates Myelin Sheath Thickness. *Science*.
755 304:700–703. doi:10.1126/science.1095862.

756 Micheva, K.D., D. Wolman, B.D. Mensh, E. Pax, J. Buchanan, S.J. Smith, and D.D. Bock. 2016. A large fraction
757 of neocortical myelin ensheathes axons of local inhibitory neurons. *Elife*. 5:e15784.
758 doi:10.7554/eLife.15784.

759 Misgeld, T., R.W. Burgess, R.M. Lewis, J.M. Cunningham, J.W. Lichtman, and J.R. Sanes. 2002. Roles of
760 neurotransmitter in synapse formation. *Neuron*. 36:635–648. doi:10.1016/S0896-6273(02)01020-6.

761 Monk, K.R., M.L. Feltri, and C. Taveggia. 2015. New insights on schwann cell development. *Glia*. 63:1376–
762 1393. doi:10.1002/glia.22852.

763 Mount, C.W., and M. Monje. 2017. Wrapped to Adapt: Experience-Dependent Myelination. *Neuron*.

95:743–756. doi:10.1016/j.neuron.2017.07.009.

Nave, K.-A., and B.D. Trapp. 2008. Axon-glial signaling and the glial support of axon function. *Annu. Rev. Neurosci.* 31:535–561. doi:10.1146/annurev.neuro.30.051606.094309.

Nave, K.A. 2010. Myelination and support of axonal integrity by glia. *Nature*. 468:244–252. doi:10.1038/nature09614.

Nave, K.A., and J.L. Salzer. 2006. Axonal regulation of myelination by neuregulin 1. *Curr. Opin. Neurobiol.* 16:492–500. doi:10.1016/j.conb.2006.08.008.

Ogata, T., S. Iijima, S. Hoshikawa, T. Miura, S. Yamamoto, O. Hiromi, K. Nakamura, and S. Tanaka. 2004. Opposing Extracellular Signal-Regulated Kinase and Akt Pathways Control Schwann Cell Myelination. *J. Neurosci.* 24:6724–6732. doi:10.1523/JNEUROSCI.5520-03.2004.

Passini, M.A., and J.H. Wolfe. 2001. Widespread gene delivery and structure -specific patterns of expression in the brain after intraventricular injections of neonatal mice with an adeno-associated virus vector. *J. Virol.* 75:12382–12392. doi:10.1128/jvi.75.24.12382-12392.2001.

Pereira, J.A., F. Lebrun-Julien, and U. Suter. 2012. Molecular mechanisms regulating myelination in the peripheral nervous system. *Trends Neurosci.* 35:123–134. doi:10.1016/j.tins.2011.11.006.

Peters, A., S.L. Palay, and H.D.F. Webster. 1991. The neurones and supporting cells, in the fine structure of the nervous system. New York : Oxford University Press, 1991. 496.

Plucińska, G., D. Paquet, A. Hruscha, L. Godinho, C. Haass, B. Schmid, and T. Misgeld. 2012. In vivo imaging of disease-related mitochondrial dynamics in a vertebrate model system. *J. Neurosci.* 32:16203–16212. doi:10.1523/JNEUROSCI.1327-12.2012.

Rasband, M.N., and E. Peles. 2016. The nodes of Ranvier: Molecular assembly and maintenance. *Cold Spring Harb. Perspect. Biol.* 8:1–16. doi:10.1101/cshperspect.a020495.

Rios, J.C., C. V Melendez-Vasquez, S. Einheber, M. Lustig, M. Grumet, J. Hemperly, E. Peles, and J.L. Salzer. 2000. Contactin-associated protein (Caspr) and contactin form a complex that is targeted to the paranodal junctions during myelination. *J. Neurosci.* 20:8354–8364. doi:10.1523/jneurosci.20-22-08354.2000.

Roche, S.L., D.L. Sherman, K. Dissanayake, G. Soucy, A. Desmazieres, D.J. Lamont, E. Peles, J.-P. Julien, T.M. Wishart, R.R. Ribchester, P.J. Brophy, and T.H. Gillingwater. 2014. Loss of glial neurofascin155 delays developmental synapse elimination at the neuromuscular junction. *J. Neurosci.* 34:12904–18. doi:10.1523/JNEUROSCI.1725-14.2014.

Roll-Mecak, A. 2019. How cells exploit tubulin diversity to build functional cellular microtubule mosaics. *Curr. Opin. Cell Biol.* 56:102–108. doi:10.1016/j.ceb.2018.10.009.

Rossi, J., N. Balthasar, D. Olson, M. Scott, E. Berglund, C.E. Lee, M.J. Choi, D. Lauzon, B.B. Lowell, and J.K. Elmquist. 2011. Melanocortin-4 receptors expressed by cholinergic neurons regulate energy balance and glucose homeostasis. *Cell Metab.* 13:195–204. doi:10.1016/j.cmet.2011.01.010.

Rousse, I., and R. Robitaille. 2006. Calcium signaling in Schwann cells at synaptic and extra-synaptic sites: active glial modulation of neuronal activity. *Glia*. 54:691–699. doi:10.1002/glia.

Sagasti, A., M.R. Guido, D.W. Raible, and A.F. Schier. 2005. Repulsive interactions shape the morphologies and functional arrangement of zebrafish peripheral sensory arbors. *Curr. Biol.* 15:804–814. doi:10.1016/j.cub.2005.03.048.

Schafer, D.P., A.W. Custer, P. Shrager, and M.N. Rasband. 2006. Early events in node of Ranvier formation during myelination and remyelination in the PNS. *Neuron Glia Biol.* 2:69–79. doi:10.1017/S1740925X06000093.

807 Schindelin, J., I. Arganda-Carreras, E. Frise, V. Kaynig, M. Longair, T. Pietzsch, S. Preibisch, C. Rueden, S.
808 Saalfeld, B. Schmid, J.Y. Tinevez, D.J. White, V. Hartenstein, K. Eliceiri, P. Tomancak, and A. Cardona.
809 2012. Fiji: An open-source platform for biological-image analysis. *Nat. Methods*. 9:676–682.
810 doi:10.1038/nmeth.2019.

811 Sherman, D.L., and P.J. Brophy. 2000. A tripartite nuclear localization signal in the PDZ-domain protein L-
812 periaxin. *J. Biol. Chem.* 275:4537–4840. doi:10.1074/jbc.275.7.4537.

813 Simons, M., and J. Trotter. 2007. Wrapping it up: The cell biology of myelination. *Curr. Opin. Neurobiol.*
814 17:533–540. doi:10.1016/j.conb.2007.08.003.

815 Stevens, B., and R.D. Fields. 2000. Response of Schwann cells to action potentials in development. *Science*.
816 287:2267–2271. doi:10.1126/science.287.5461.2267.

817 Stevens, B., S. Porta, L.L. Haak, V. Gallo, and R.D. Fields. 2002. Adenosine: A neuron-glial transmitter
818 promoting myelination in the CNS in response to action potentials. *Neuron*. 36:855–868.
819 doi:10.1016/S0896-6273(02)01067-X.

820 Tapia, J.C., and J.W. Lichtman. 2012. Synapse Elimination. *In* Fundamental Neuroscience: Fourth Edition.
821 437–455.

822 Tapia, J.C., J.D. Wylie, N. Kasthuri, K.J. Hayworth, R. Schalek, D.R. Berger, C. Guatimosim, H.S. Seung, and
823 J.W. Lichtman. 2012. Pervasive synaptic branch removal in the mammalian neuromuscular system at
824 birth. *Neuron*. 74:816–829. doi:10.1016/j.neuron.2012.04.017.

825 Taveggia, C., M.L. Feltri, and L. Wrabetz. 2010. Signals to promote myelin formation and repair. *Nat. Rev.*
826 *Neurol.* 6:276–287. doi:10.1038/nrneurol.2010.37.

827 Taveggia, C., G. Zanazzi, A. Petrylak, H. Yano, J. Rosenbluth, S. Einheber, X. Xu, R.M. Esper, J.A. Loeb, P.
828 Shrager, M. V. Chao, D.L. Falls, L. Role, and J.L. Salzer. 2005. Neuregulin-1 type III determines the
829 ensheathment fate of axons. *Neuron*. 47:681–694. doi:10.1016/j.neuron.2005.08.017.

830 Tomassy, G.S., D.R. Berger, H.H. Chen, N. Kasthuri, K.J. Hayworth, A. Vercelli, H.S. Seung, J.W. Lichtman,
831 and P. Arlotta. 2014. Distinct profiles of myelin distribution along single axons of pyramidal neurons
832 in the neocortex. *Science*. 344:319–324. doi:10.1126/science.1249766.

833 Turney, S.G., and J.W. Lichtman. 2012. Reversing the outcome of synapse elimination at developing
834 neuromuscular junctions in vivo: Evidence for synaptic competition and its mechanism. *PLoS Biol.*
835 10:e1001352. doi:10.1371/journal.pbio.1001352.

836 Vabnick, L., and P. Shrager. 1998. Ion channel redistribution and function during development of the
837 myelinated axon. *J. Neurobiol.* 37:80–96. doi:10.1002/(SICI)1097-4695(199810)37:1<80::AID-
838 NEU7>3.0.CO;2-4.

839 Velanac, V., T. Unterbarnscheidt, W. Hinrichs, M.N. Gummert, T.M. Fischer, M.J. Rossner, A. Trimarco, V.
840 Brivio, C. Taveggia, M. Willem, C. Haass, W. Möbius, K.A. Nave, and M.H. Schwab. 2012. Bace1
841 processing of NRG1 type III produces a myelin-inducing signal but is not essential for the stimulation
842 of myelination. *Glia*. 60:203–217. doi:10.1002/glia.21255.

843 Voyvodic, J.T. 1989. Target size regulates calibre and myelination of sympathetic axons. *Nature*. 342:430–
844 433. doi:10.1038/342430a0.

845 Walsh, M.K., and J.W. Lichtman. 2003. In vivo time-lapse imaging of synaptic takeover associated with
846 naturally occurring synapse elimination. *Neuron*. 37:67–73. doi:10.1016/S0896-6273(02)01142-X.

847 Woo, T.U.W., and A.L. Crowell. 2005. Targeting synapses and myelin in the prevention of schizophrenia.
848 *Schizophr. Res.* 73:193–207. doi:10.1016/j.schres.2004.07.022.

849 Yamamoto, K., A.C. Merry, and A.A.F. Sima. 1996. An orderly development of paranodal axoglial junctions

and bracelets of Nageotte in the rat sural nerve. *Dev. Brain Res.* 96:36–45. doi:10.1016/0165-3806(96)00072-7.

Yamashita, N. 2019. Retrograde signaling via axonal transport through signaling endosomes. *J. Pharmacol. Sci.* 141. doi:10.1016/j.jphs.2019.10.001.

Yin, X., R.C. Baek, D.A. Kirschner, A. Peterson, Y. Fujii, K.A. Nave, W.B. Macklin, and B.D. Trapp. 2006. Evolution of a neuroprotective function of central nervous system myelin. *J. Cell Biol.* 172:469–479. doi:10.1083/jcb.200509174.

Zhang, Y., Y. Bekku, Y. Dzhashiashvili, S. Armenti, X. Meng, Y. Sasaki, J. Milbrandt, and J.L. Salzer. 2012. Assembly and maintenance of nodes of Ranvier rely on distinct sources of proteins and targeting mechanisms. *Neuron*. 73:92–107. doi:10.1016/j.neuron.2011.10.016.

Zonta, B., A. Desmazieres, A. Rinaldi, S. Tait, D.L. Sherman, M.F. Nolan, and P.J. Brophy. 2011. A critical role for neurofascin in regulating action potential initiation through maintenance of the axon initial segment. *Neuron*. 69:945–956. doi:10.1016/j.neuron.2011.02.021.

ABBREVIATIONS

AAV: adeno-associated virus

AChR: acetylcholine receptor

BTX: bungarotoxin

Caspr1: contactin-associated protein 1

CBD: cargo-binding domain

CNS: central nervous system

CNTN2: contactin-2

din: doubly innervated NMJ

dpf: days post fertilization

FRAP: fluorescence recovery after photobleaching

KHC: kinesin-1 heavy chain

KO: knock-out

Nav: voltage-gated sodium channel

NMJ: neuromuscular junction

MPZ: myelin protein zero

Nrg1: Neuregulin-1

pERK: phosphorylated form of extracellular signal–regulated kinase 1/2

PNS: peripheral nervous system

P: postnatal day

SC: Schwann cell

sin: singly innervated NMJ

FIGURE LEGENDS

Figure 1| Myelination coincides with axon remodeling during the second postnatal week.

(A) Schematic of thoracic nerve-muscle explant indicating anatomy of motor axons (dark gray). 'Stem axon' in intercostal nerve; 'soma', motor neuron cell body in spinal cord; triangularis sterni muscle (pink); sternum and ribs (light gray). Boxed area of 'terminal branches' is schematized in more detail in (B). **(B)** Schematic of terminal branches of motor neurons (dark gray), postsynaptic acetylcholine receptors ('NMJ'; blue). Din, doubly innervated NMJ, black arrowheads point to two 'competing branches' leading to the same NMJ; sin, singly innervated NMJ, 'winner branch'. Regions of nodes of Ranvier: paranodes (green), node (red), juxtaparanodes (cyan). Schwann cells myelinate axons in internodal regions (magenta). **(C)** P7, 9, 11 *triangularis sterni* muscles of *Thy1*-YFP16 mice (axon, white), immunostained for Caspr (green), postsynaptic acetycholine receptors (BTX, blue). Inset shows emerging paranodal Caspr cluster at P9. Corresponding schematics to the right, axons (gray) and Caspr-positive paranodes (green). Black arrowheads point to two axons leading to the same NMJ. **(D)** Quantification of the percentage of doubly innervated NMJs at P7, P9, and P11 ($n \geq 5$ mice, ≥ 100 NMJs per animal, gray) and the percentage of Caspr-positive terminal branches among singly innervated NMJs ($n \geq 5$ mice, ≥ 100 NMJs per animal, gray) and the percentage of Caspr-positive terminal branches among singly innervated NMJs ($n \geq 7$ mice, ≥ 30 branches per animal, green). **(E)** Nodes of Ranvier and myelin components: Immunostaining for Caspr (green, paranode), Nav (red, nodal region), CNTN2 (cyan, juxtaparanode) and MPZ (magenta, myelin) in single terminal axon branches of Thy1-XFP mice (axons, white). **(F)** Quantification of the percentage of myelin initiation on winner (singly innervating, 'sin') or competing (doubly innervating, 'din') terminal axon branches for Caspr (green), Nav (red), CNTN2 (cyan), or MPZ (magenta; $n \geq 5$ mice per group, ≥ 50 branches). Data, mean ± SEM in (D), mean + SEM in (F). *, $P < 0.05$; **, $P < 0.01$, Mann-Whitney test. Scale bars, 10 µm in (C) overview, 2 µm in (C) inset and (E).

Figure 2| Nodes on competing branches are immature compared to those on winner branches. **(A)** Live image of motor axons in P11 *Thy1*-Caspr-GFP (green) x *Thy1*-OFP3 (axon, white) nerve-muscle explant; dashed boxes indicate location of control (Ctrl) and photobleached (FRAP) nodes. Images on the right are taken before, directly after photobleaching, and 3 hours (h) later. Fire look-up table on the right. **(B)** Quantification of Caspr-GFP recovery rate comparing winner branches (sin) of different developmental ages (6 weeks, wk *vs.* P9-11) and different competition status at the same developmental age (P9-11 sin, din, stem; n ≥ 13 axons, ≥ 10 mice per group). **(C)** Live image of axon branches in P11 *Thy1*-β1-Nav-GFP (red) x *Thy1*-OFP3 (axon, white) nerve-muscle explant; dashed boxes and images on right as in (A). **(D)** Quantification of β1-Nav-GFP recovery rate as in (B; n ≥ 9 axons, ≥ 5 mice per group). 'Din', doubly innervating competing branch; 'sin', singly innervating winner branch. Data, mean + SEM. *, $P < 0.05$; **, $P < 0.01$; ****, $P < 0.0001$, Mann-Whitney test; outliers identified with Tukey's test. Scale bars, 10 µm in (A) and (C) overview, 2 µm in insets.

Figure 3| Myelination of competing branches neither biases competition nor reflects axon diameter.

(A) Image of a fixed *triangularis sterni* muscle of a *ChAT*-IRES-Cre x *Thy1*-Brainbow-1.1 mouse. Motor units labeled with distinct fluorescence (axon, orange and white) and immunostained for Caspr (green); arrowheads point to competing branches and asterisk marks a pruning axon. Inset shows enlarged dashed box with emerging dotty and more mature paranodal structures. **(B)** Quantification of Caspr immunostaining vs. synaptic territory of competing branches (n ≥ 78 axons per group from a total of 69 mice). **(C)** Graph of measured myelination patterns on paired competing branches vs. the calculated distribution assuming random myelin initiation. Winner is an axon branch > 50% territory, loser ≤ 50% territory. **(D)** Quantification of an axon's diameter vs. its synaptic territory in axon branches either with (green) or without Caspr-immunostaining (gray; n ≥ 10 axons, ≥ 7 mice per group). **(E)** Quantification of

the diameter of stretches on retreating axons with (magenta) or without MPZ-immunostaining (gray; n ≥ 8 axons, ≥ 4 mice per group) **(F, G)** Images of *Thy1*-XFP terminal branches (axons, white) stained for Caspr (green) and MPZ (magenta). Schematics to the right depict (F) a myelinated winning branch (black) vs. a pruning axon (gray; asterisk) without nodes; and (G) a rare example of a myelinated retreating branch (gray; asterisk) and its winning MPZ- and Caspr-negative competitor (black). 'Rebu', retraction bulbs; 'sin', winner axons. Data, mean ± SEM. **, $P < 0.01$, Mann-Whitney test. Scale bars, 10 µm in (A), (F) and (G).

Figure 4| Neurotransmission and spastin differentially affect myelination and microtubular mass.

(A) Schematic of experimental design. *Thy1*-YFP16 mice were unilaterally injected with BTX ('BTX inj', orange) into the thoracic wall at P7, resulting in local blockade of acetylcholine receptors. Fixed ipsi- and contralateral muscles are post-hoc stained at P9 with BTX (blue) and immunostained for Caspr (green). **(B)** Contralateral control muscle, and **(C)** ipsilateral BTX-injected muscle; axons (*Thy1*-YFP16, white), Caspr immunostaining (green), *post hoc* stained BTX (blue), injected BTX (orange). Schematics below depict motor neurons (gray) and Caspr paranodes (green); black arrowheads point to two competing axons leading to the same NMJ. **(D)** Quantification of doubly innervated NMJs at P9 following BTX-injection (n = 8 mice, ≥ 50 axons per animal). **(E)** Quantification of Caspr-positive competing ('din') and winner ('sin') axon branches from BTX-injected muscles *vs.* controls (n = 6 mice, ≥ 32 axons per side of animal). **(F)** Images of competing ('din') and winner ('sin') terminal branches following BTX injection ('BTX inj', orange) and post-hoc staining at P9 with BTX (blue) and βIII-tubulin (white). **(G)** Quantification of βIII-tubulin intensity (x-fold normalized to *Thy1*-YFP16; n ≥ 5 mice, n ≥ 20 axons per side of animal). **(H, I)** P9 *triangularis sterni* muscle of (H) littermate wild-type control (WT) and (I) spastin KO mouse. Axons immunostained for Caspr (green) and βIII-tubulin (white). Corresponding schematics below, axons (gray) and Caspr-positive paranodes (green). Black arrowheads point to two axons innervating the same NMJ. **(J)** Quantification of

doubly innervated NMJs in P9 spastin KO animals compared to WT littermates (n ≥ 5 mice, n ≥ 70 axons per animal). **(K)** Quantification of Caspr-positive terminal branches in P9 spastin KO compared to WT littermates (n ≥ 7 mice, n ≥ 33 axons per animal). **(L)** Images of competing ('din') and winner ('sin') terminal branches in spastin WT and KO littermates, immunostained for βIII-tubulin (white). **(M)** Quantification of βIII-tubulin intensity (x-fold normalized to *Thy1*-YFP16) in spastin KO *vs.* WT littermates (n ≥ 5 mice, n ≥ 13 axons per animal). 'Din', competing axons; 'sin', winner axons. Data, mean + SEM. Mann-Whitney test *, P < 0.05; **, P < 0.01. Scale bars, 10 µm in (B), (C), (H) and (I), 5 µm in (F) and (L).

Figure 5| Axonal transport limits myelination onset in terminal motor axon branches.

(A) Schematic of experimental design. AAV9-*hSyn*-iCre-p2a-KHC-CBD was injected at P2 into the 3rd ventricle of YFP reporter mice. Muscles were analyzed at P9. **(B)** Quantification of axonal GFP particle transport in β1-Nav-GFP animals (n ≥ 16 axons, ≥ 5 mice per group). **(C)** Image of AAV9-hSyn-iCre-p2a-KHC-CBD-injected P9 triangularis sterni muscle of a YFP reporter mouse immunostained for Caspr (green) and βIII-tubulin (white). KHC-CBD is overexpressed in iCre-induced recombined YFP reporter-positive axons (red). Schematic on the right depicts YFP-positive (red) and -negative motor units (gray), Caspr paranodes (green). **(D)** Quantification of Caspr-immunostaining on YFP-negative and -positive terminal axon branches at P9 (n ≥ 5 mice per group, n ≥ 39 axons per mouse). 'Din', competing axons; 'sin', winner axons. Data, mean + SEM. *, P < 0.05; **, P < 0.01; ****, P < 0.0001, Mann-Whitney test. Outlier determined by Tukey test. Scale bar, 20 µm in (C).

Figure 6| Nrg1 type III transgenic mice show premature myelination initiation.

(A, B) P9 spinal cord of WT control (A) and *Thy1*-Nrg1 type III-HA (B) littermates. Sections stained for HA-tag (red) and neurotrace (cyan). Dashed boxes enlarged on the right, showing magnified single channel of neurotrace (cyan) and HA staining (red). **(C, D)** Confocal images of P9 triangularis sterni muscles from (C)

WT and (D) Thy1-Nrg1 type III-HA littermates immunostained for βIII-tubulin (white) and Caspr (green). Schematics below, motor neurons (gray), Caspr paranodes (green). Black arrowheads point to two axons leading to the same NMJ. **(E, F)** Quantification of the percentage of (E) doubly innervated NMJs and (F) Caspr-positive terminal branches in P7 and P9 WT vs. transgenic *Thy1*-Nrg1 type III littermates. (E, n ≥ 3 mice per genotype, ≥ 99 axons per animal; F, n ≥ 3 mice per genotype, ≥ 40 axons per animal). 'Din', competing axons; 'sin', winner axons. Data, mean + SEM. *, P < 0.05; **, P < 0.01, Mann-Whitney test. Scale bars, 10 µm in (A – D).

Figure 7| Nrg1 type III is more concentrated on singly innervating terminal branches.

(A, B) *Plp*-GFP x *Thy1*-Nrg1 type III-HA mouse immunostained for neurofilament (NF, white) in P9 triangularis sterni muscle. A stacked overview of competing ('din') vs. winner branches ('sin'); dashed boxes enlarged in (B), showing magnified single optical sections of HA staining (red) with GFP labeled Schwann cells (green). **(C)** Quantification of HA staining on doubly vs. singly innervating branches in *Thy1*-Nrg1 type III animals (n = 8 mice per genotype, ≥ 13 axons per animal). **(D, E)** *Plp*-GFP x *Thy1*-Nrg1 type III-HA mice immunostained for βIII-tubulin (white) in P9 triangularis sterni muscle. A stacked overview (D) of competing ('din') vs. winner branches ('sin'); dashed boxes enlarged in (E), showing magnified single optical sections of pERK staining (magenta) with GFP labeled Schwann cells (green). **(F)** Quantification of pERK staining around doubly vs. singly innervating branches in *Thy1*-Nrg1 type III animals (n = 5 mice per genotype, ≥20 axons per animal). **(G)** Quantification of pAKT immunostaining around doubly vs. singly innervating branches in *Thy1*-Nrg1 type III animals, normalized to singly innervating branches (≥ 20 axons per group in n = 5 mice). **(H)** Quantification of HA signal in singly innervating axons in BTX injected triangularis sterni muscle vs. uninjected control side (≥ 13 axons per group in n = 6 mice). **(I)** Quantification of pERK signal in Schwann cells surrounding singly innervating axons in BTX injected triangularis sterni muscle vs. uninjected control side (≥ 36 axons per group in n = 5 mice). **(J)** BTX intensity measured in wild-type and *Thy1*-Nrg1 type III transgenic animals (wild-type: 698 ± 67 A.U., *Thy1*-Nrg1 type III: 747 ± 43 A.U.,

n ≥ 16 NMJ per animal, n ≥ 5 mice per group). **(K)** Area of BTX-stained endplate measured in wild-type and *Thy1*-Nrg1 type III transgenic animals (wild-type: 195 ± 13 µm2, *Thy1*-Nrg1 type III: 203 ± 22 µm2, n ≥ 16 NMJ per animal, n ≥ 5 mice per group). **(L)** Quantification of the proportions of NMJ morphology, categorized into 'broken', 'holes' and 'plaque' (n ≥ 5 mice per group, ≥ 14 NMJ per animal). 'Din', competing axons; 'sin', winner axons. Data, mean + SEM. *, P < 0.05; **, P < 0.01, Mann-Whitney test. Scale bars, 10 µm in (A) and (D); 5 µm in (B) and (E).

SUPPLEMENTARY FIGURE LEGENDS

Figure S1| Characterization of *Thy1*-Caspr-GFP and *Thy1*-β1-Nav-GFP mice.

(A) Confocal image of P9 *Thy1*-Caspr-GFP (native GFP, green) intercostal axons (βIII-tubulin, white) immunostained for Caspr (red). Dashed boxes enlarged below show single channels. The percentage of GFP-positive paranodes nodes was stable across development, suggesting consistent labeling of a neuronal subset (P9-11: 65 ± 8 % of all paranodal structures; 6 weeks: 73 ± 9 %; P = 0.7, Mann-Whitney test; n = 4 mice per age group, ≥ 44 nodes per animal). **(B)** *Triangularis sterni* muscle of a P9 *Thy1*-Caspr-GFP mouse immunostained for Caspr (red) and axons (βIII- tubulin, white). Dashed boxes enlarged below, showing Caspr/GFP double-positive (i) and Caspr only-positive paranode (ii). Expression of the Caspr-GFP transgene did not detectably influence the degree of double innervation (WT: 9 ± 1 % *vs.* Caspr-GFP: 12 ± 2 %; P = 0.4, Mann-Whitney test; n = 3 mice per genotype, ≥ 136 axons per animal) or myelination on terminal axon branches at P9 (winner branches - WT: 32 ± 2 % *vs.* Caspr-GFP: 35 ± 8 %; competing branches - WT: 12 ± 6 % *vs.* Caspr-GFP: 7 ± 7 %; P > 0.99, Mann-Whitney test; n = 3 mice per genotype, ≥ 31 axons per animal). **(C)** Image of P9 *Thy1*-β1-Nav-GFP (native GFP, green) intercostal axons (βIII-tubulin, white) immunostained for Nav (red). Dashed boxes enlarged below show single channels. All nodes identified by immunostaining were also GFP-positive, indicating transgene expression in all motor neurons (100 ± 0 %; n = 3 mice, ≥ 40 axons per animal). **(D)** *Triangularis sterni* muscle of a P9 *Thy1*-β1-Nav-GFP mouse immunostained for Nav

(red) along terminal axon branches (βIII-tubulin, white). Insets show enlarged Nav/GFP double-positive nodes. Expression of the β1-Nav-GFP transgene did not detectably influence the degree of double innervation (WT: 11 ± 1 % *vs.* β1-Nav-GFP: 14 ± 2 %; n = 3 mice per genotype, ≥ 102 axons; P = 0.7, Mann-Whitney test; axons per animal) or myelination on terminal axon branches at P9 (winner branches - WT: 38 ± 8 % *vs.* β1-Nav-GFP: 30 ± 4 %; competing branches - WT: 19 ± 3 % *vs.* β1-Nav-GFP: 11 ± 6 %; P > 0.4, Mann-Whitney test; n = 3 mice per genotype, ≥ 31 axons per animal). 'Din', competing axons; 'sin', winner axons. Scale bars, 10 µm in (A–D) overview, 2 µm in insets.

Figure S2| Innervation and myelination status correlate with axonal tubulin content and SC length.

(A) Images of Schwann cells on singly innervating terminal branches in *Plp*-GFP (green) mouse following BTX injection on P7 vs. contralateral control side and post-hoc staining at P9 with βIII-tubulin (white). Schematics to the right depict measured terminal axon length (gray) and Schwann cell outline with cell nuclei marked with asterisks. **(B–D)** Quantification of **(B)** Schwann cell length, **(C)** terminal branch length and **(D)** Schwann cell number along singly innervating branches, showing no significant difference after BTX treatment in P9 *Plp*-GFP mice injected with BTX vs. control (≥ 10 axons per animal in n = 5 mice). **(E-F)** Quantification of **(E)** axonal Schwann cell length (din: 30 ± 2 µm; sin: 24 ± 1 µm) and **(F)** terminal branch length (din: 50 ± 4 µm; sin: 54 ± 5 µm; ≥ 16 axons per animal in n = 5 mice). **(G)** Images of competing ('din') and winner ('sin') terminal branches in P9 Thy1-YFP16 mice, without or with emerging Caspr paranodes (green) and stained βIII-tubulin (white). **(H)** Quantification of βIII-tubulin intensity (x-fold normalized to Thy1-YFP16; Caspr- n ≥ 18 axons per group in n = 3 mice). 'Din', competing axons; 'sin', winner axons. Data, mean + SEM. *, P < 0.05; **, P < 0.01; ***, P < 0.001; Mann-Whitney test. Outlier determined by Tukey test. Scale bar, 10 µm in (A) and (G).

Figure S3| AAV9 mediated spastin deletion promotes myelination on competing branches.

(A) Schematic of experimental design. AAV9-*CMV*-iCre was injected at P2 into the 3rd ventricle of spastin$^{fl/fl}$ x TdTomato reporter mice. Muscles were analyzed at P9. **(B)** Image of P9 muscle immunostained for Caspr (green) and βIII-tubulin (white). iCre-mediated deletion resulted in TdTomato-positive axons (red), presumed to lack spastin. Schematic on the right depicts TdTomato-positive (red) and -negative motor units (gray), Caspr paranodes (green). Black arrowheads point to competing axons leading to the same NMJ. **(C)** Quantification of Caspr-immunostaining on TdTomato-negative and -positive terminal branches at P9 (n ≥ 3 mice per group, n ≥ 15 axons per mouse). **(D)** Quantification of axon diameter of TdTomato-negative and -positive terminal branches at P9 (n ≥ 10 axons per group, n = 5 mice). **(E)** Schematic of experimental design. AAV9-*CMV*-iCre was injected at P2 into the 3rd ventricle of Nrg1 type III$^{fl/fl}$ x TdTomato reporter mice. Muscles were analyzed at P9. **(F)** Image of P9 muscle immunostained for Caspr (green) and βIII-tubulin (white). iCre-mediated deletion resulted in TdTomato-positive axons (red), presumed to lack Nrg1. Schematic on the right depicts TdTomato-positive (red) and -negative motor units (gray), Caspr paranodes (green). Black arrowheads point to two axons leading to the same NMJ. **(G)** Quantification of doubly innervated NMJs on TdTomato-negative and -positive terminal branches at P9 (n = 4 mice per group, ≥ 97 axons per animal). **(H)** Quantification of Caspr-immunostaining on TdTomato-negative and -positive terminal branches at P9 (n = 4 mice per group, ≥ 29 axons per animal). 'Din', competing axons; 'sin', winner axons. Data, mean + SEM. *, P < 0.05, Mann-Whitney test. Outlier determined by Tukey test. Scale bar, 10 µm in (B) and (F).

Figure S4| Microtubule-dependent axonal transport affects myelination onset.

(A–D) Whole-mount immunohistochemical staining against α-tub (white) to label axons in Tg(mbp:RFP) (magenta) transgenic zebrafish larvae injected with cntn1b:GFP as control (A, B) and cntn1b:GFP-KHC-CBD (C, D). Dashed boxes in (A, C) are enlarged in (B, D) showing mbp:RFP only. **(E)** Example of an individual

cntn1b:GFP-KHC-CBD labelled motor neuron (yellow) and its myelination (magenta). Solid arrow heads point to ends of myelin sheaths; empty arrow head points to extend of myelination along KHC-CBD expressing axons compared to control axons in the adjacent somite (unlabeled). **(F)** Length of spinal motor axons, measured between the branching-off point at the spinal cord to the axon tip (n = 7 zebrafish per group, n ≥ 29 axons per animal). **(G)** Progress of myelination expressed as percentage of mbp:RFP-positive axon length (n = 7 zebrafish per group, n ≥ 29 axons per animal). Data, mean + SEM. ***, $P < 0.001$, Mann-Whitney test. Scale bar, 50 μm in (A–E).

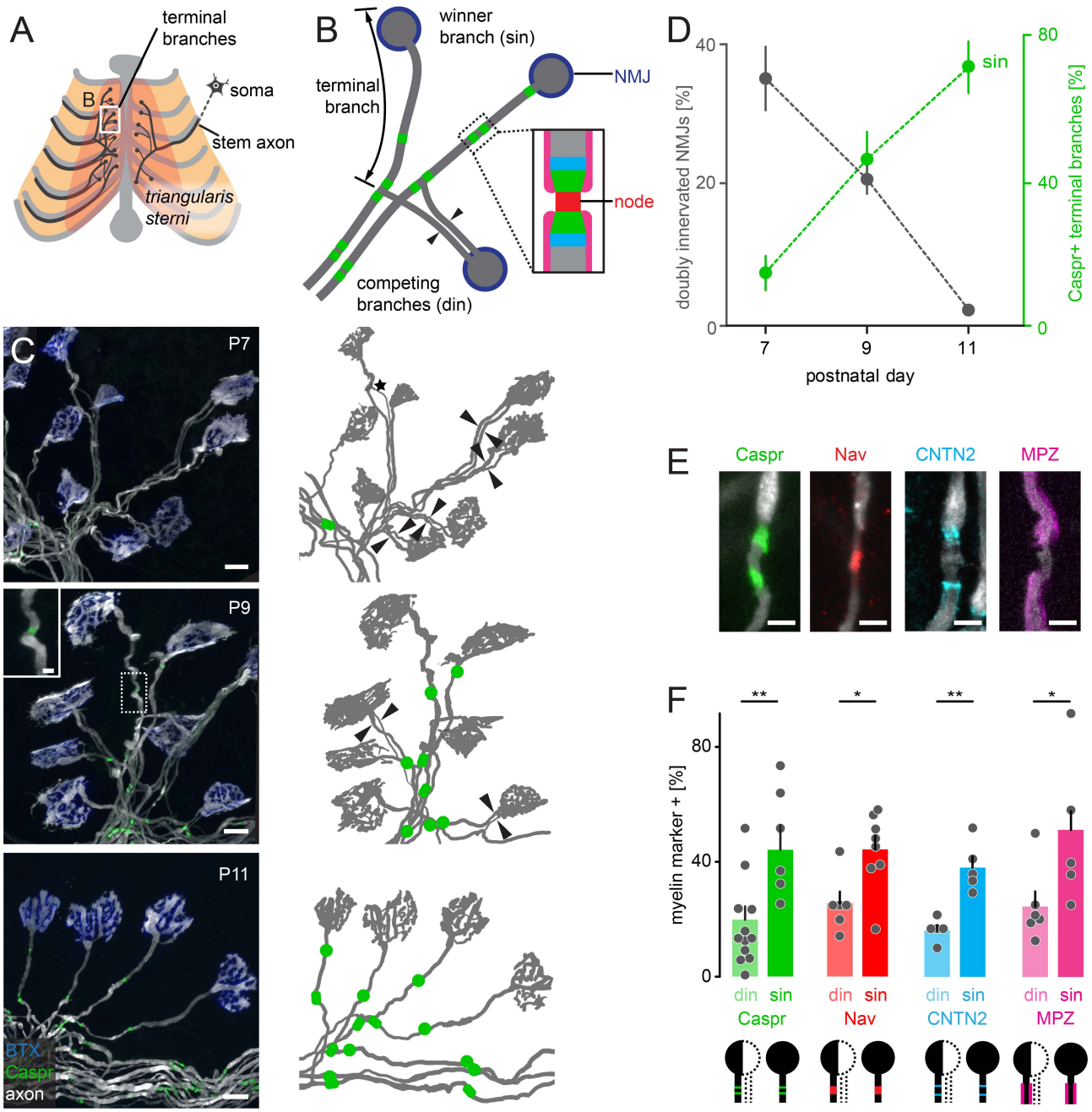

Wang et al., Figure 1

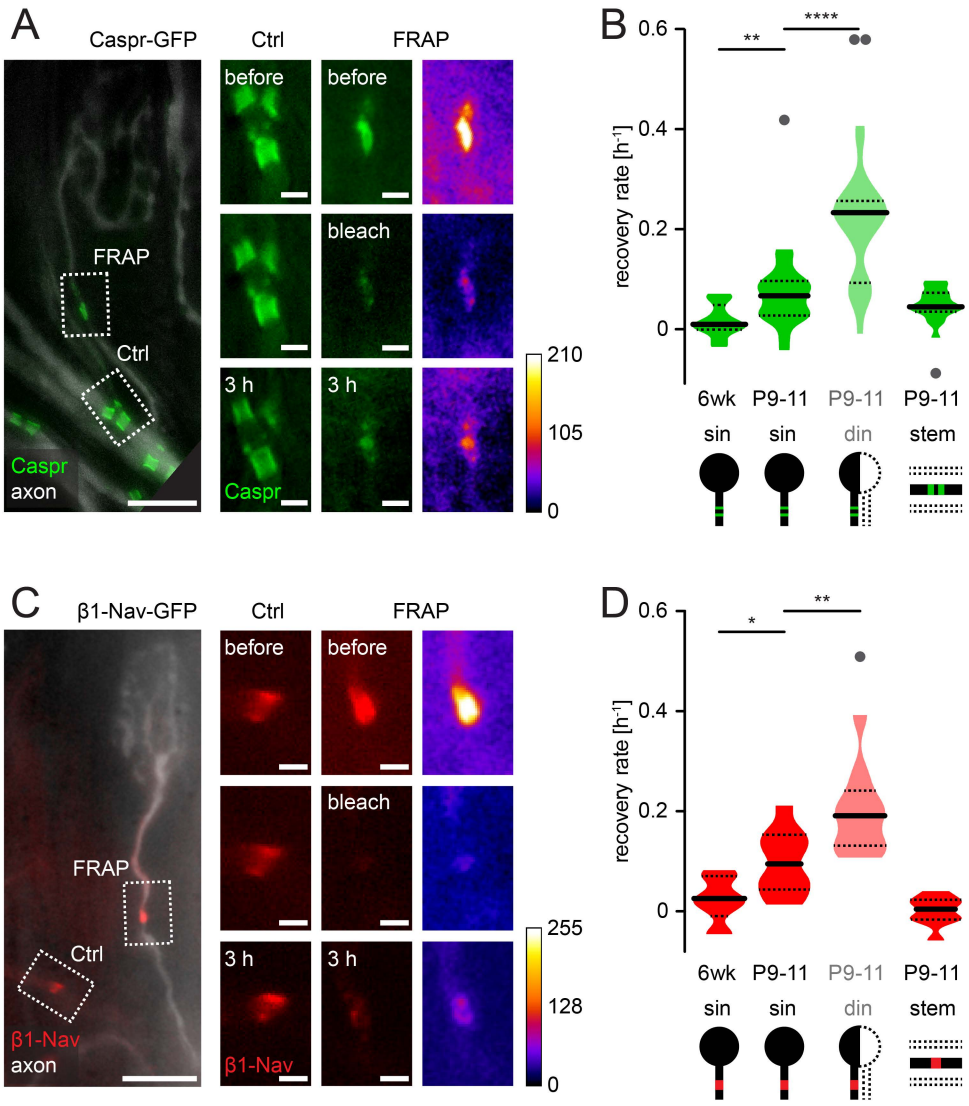

Wang et al., Figure 2

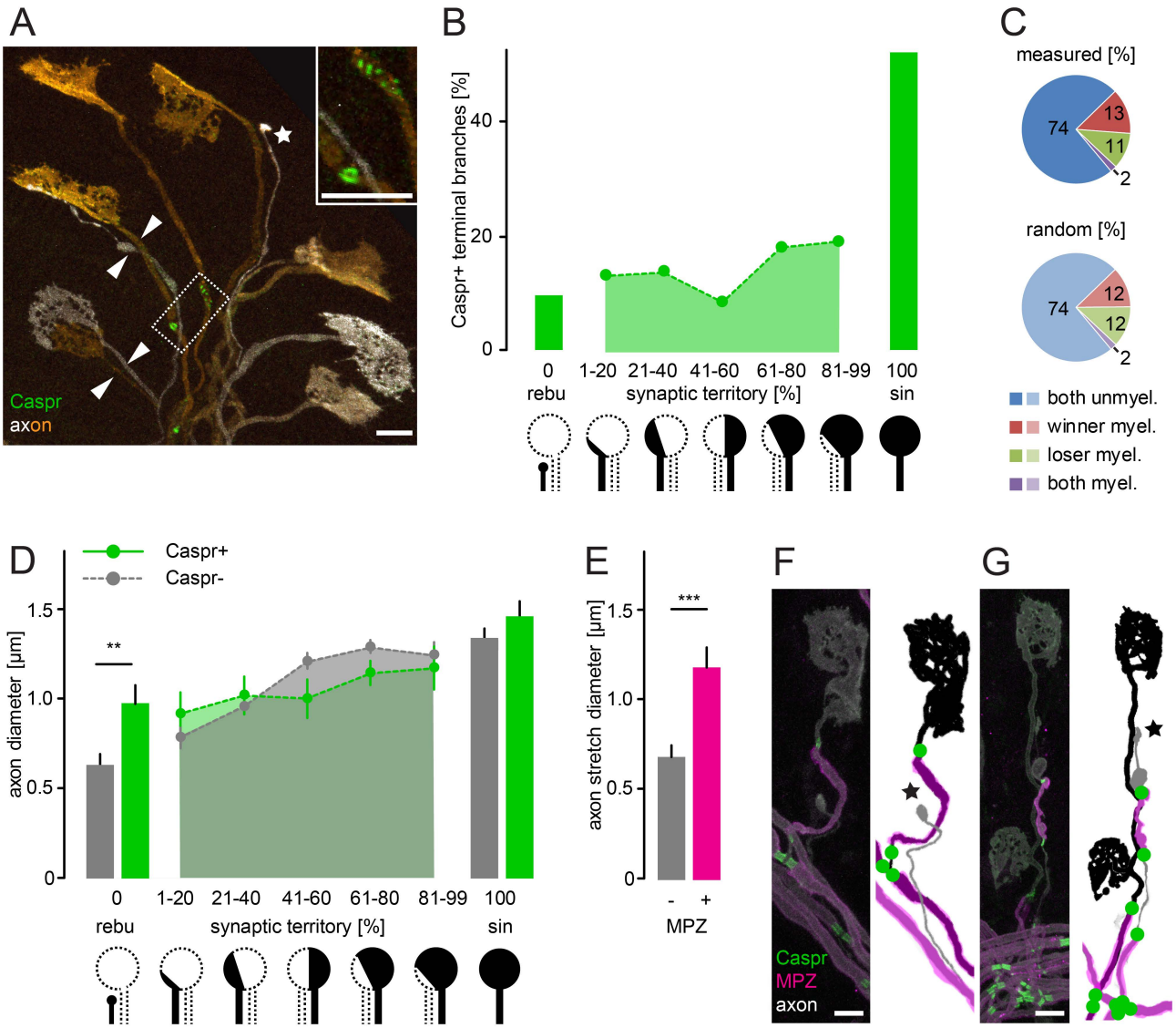

Wang et al., Figure 3

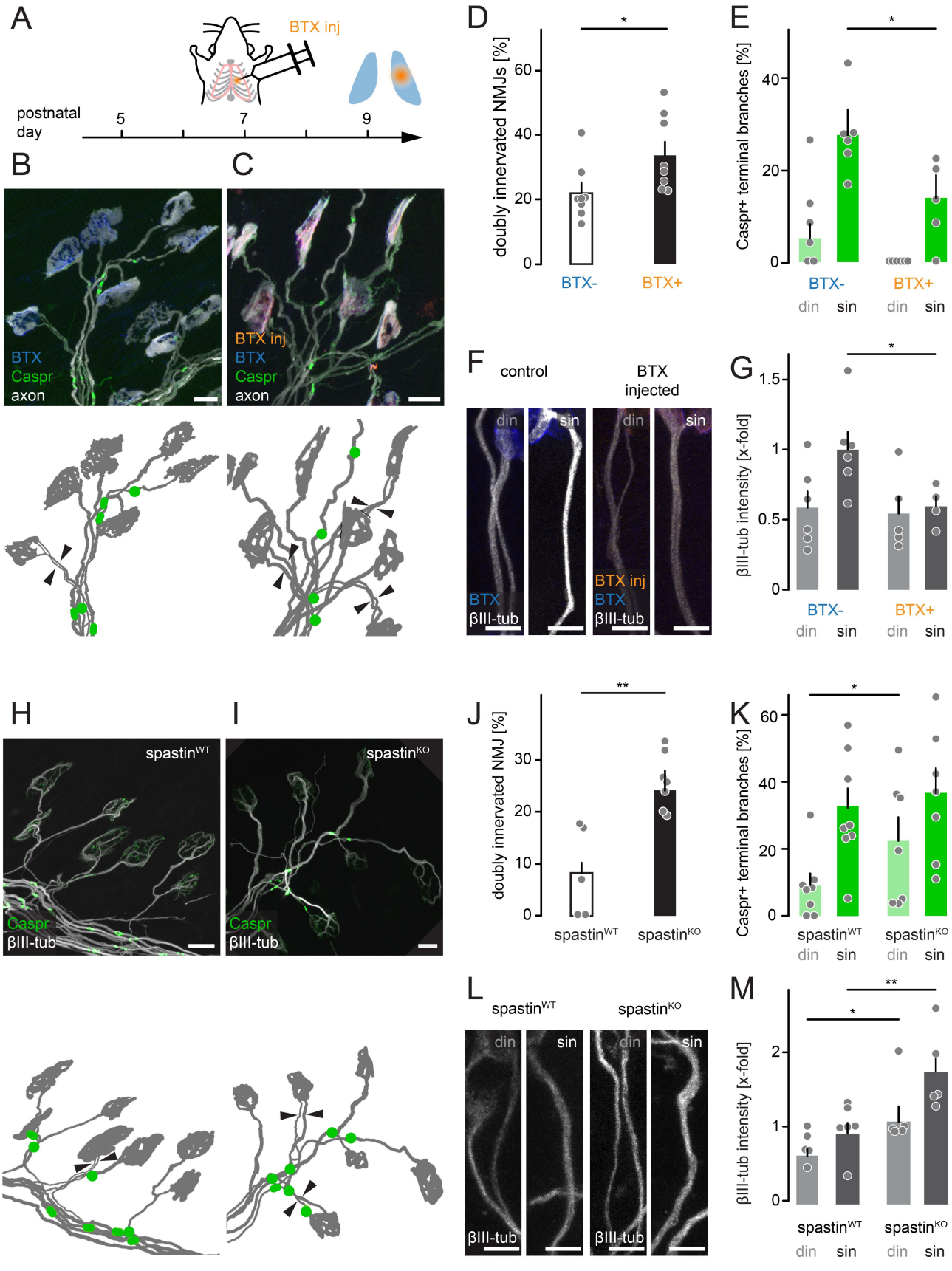

Wang et al., Figure 4

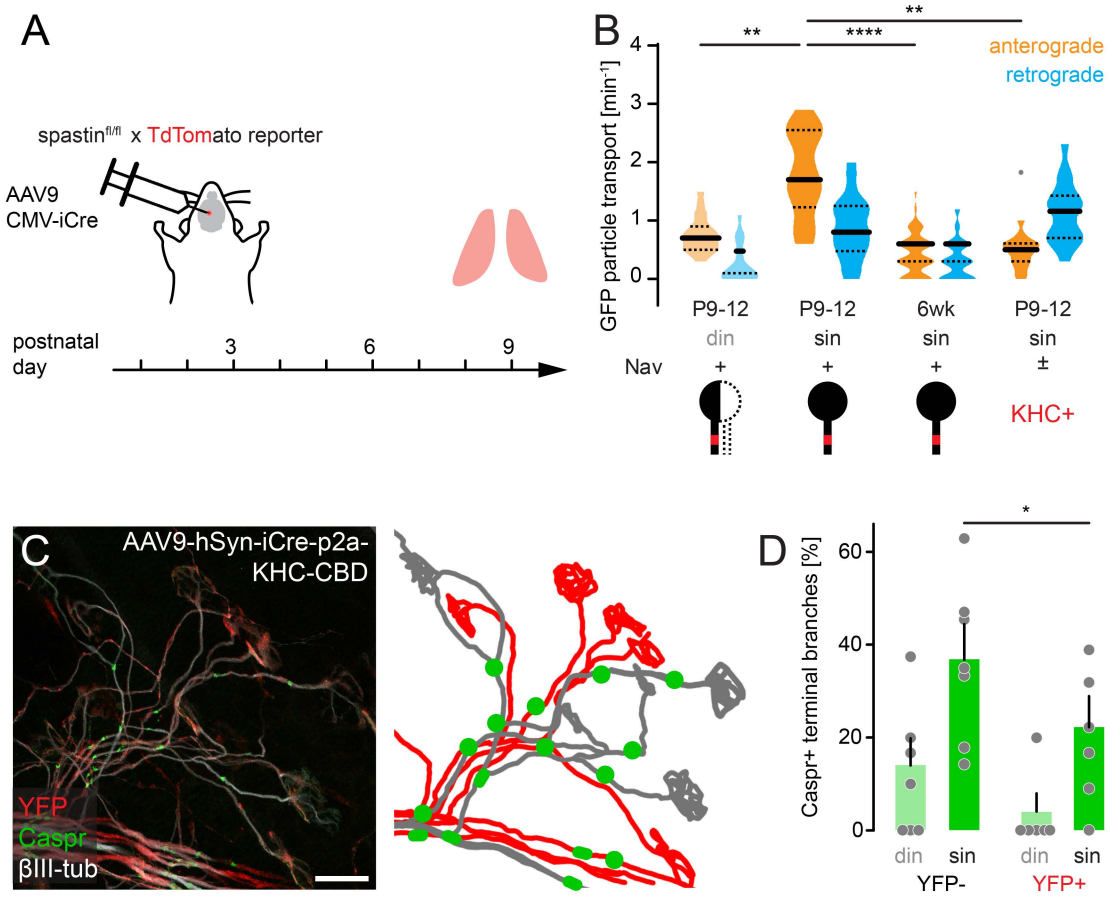

Wang et al., Figure 5

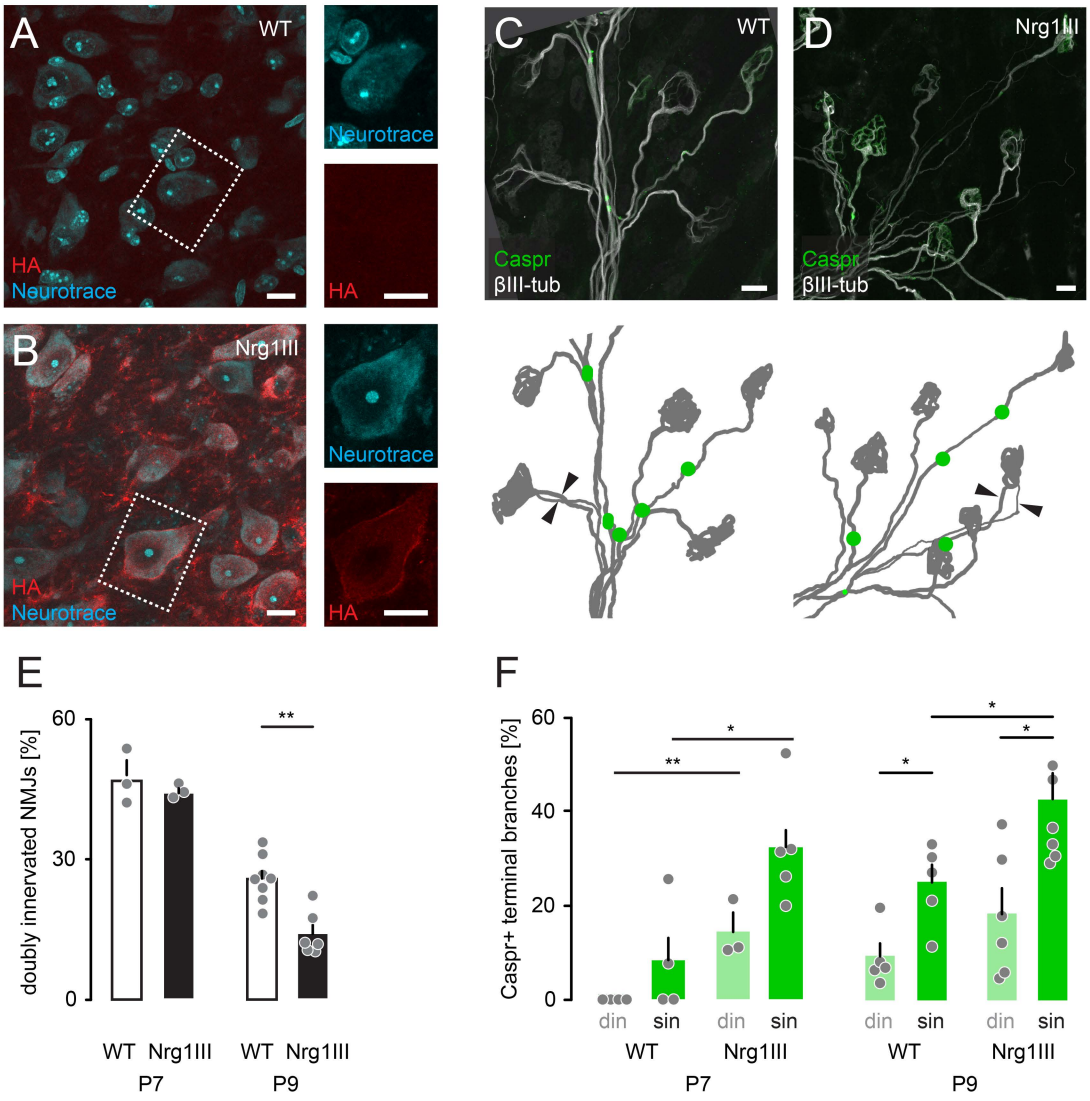

Wang et al., Figure 6

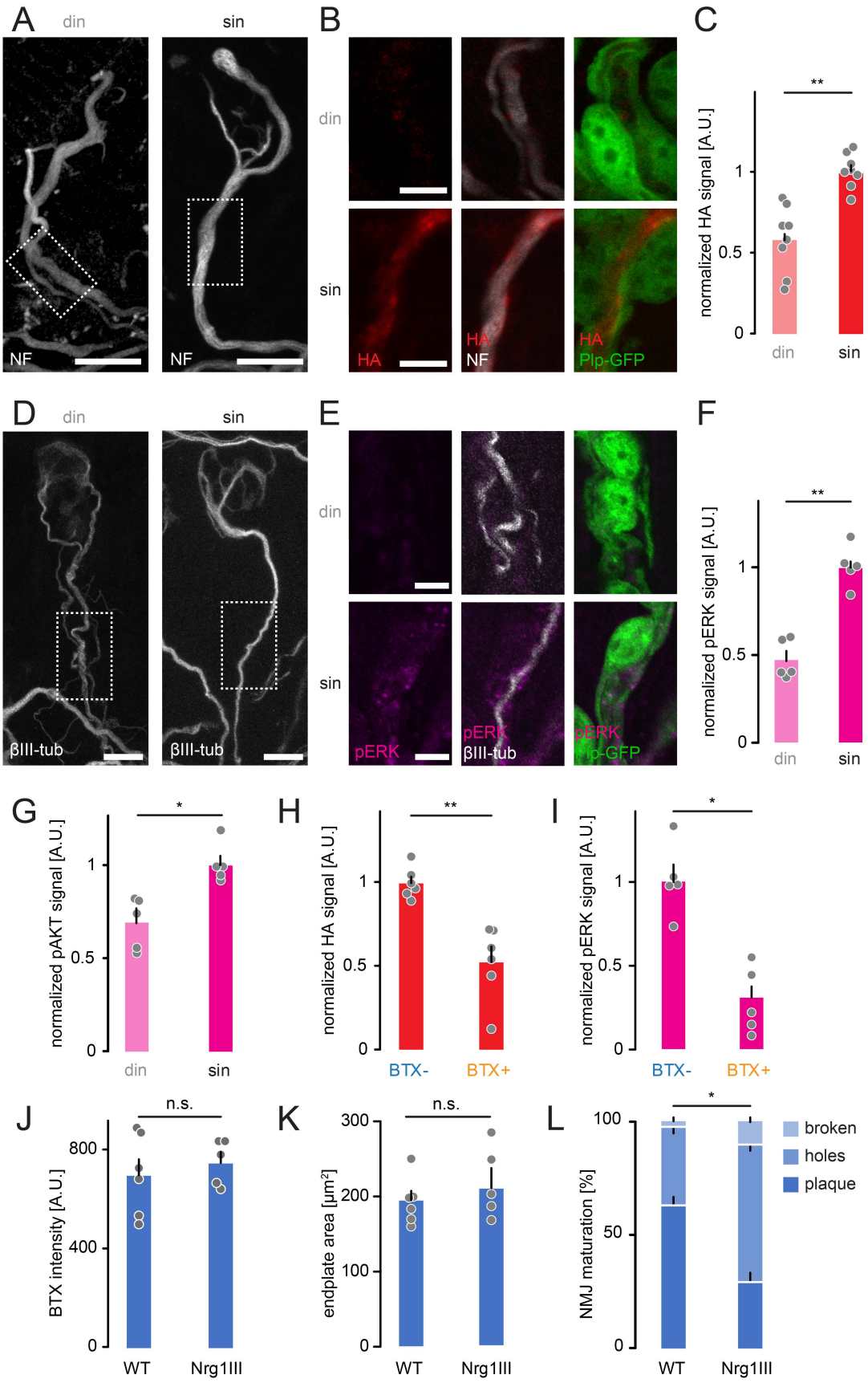

Wang et al., Figure 7

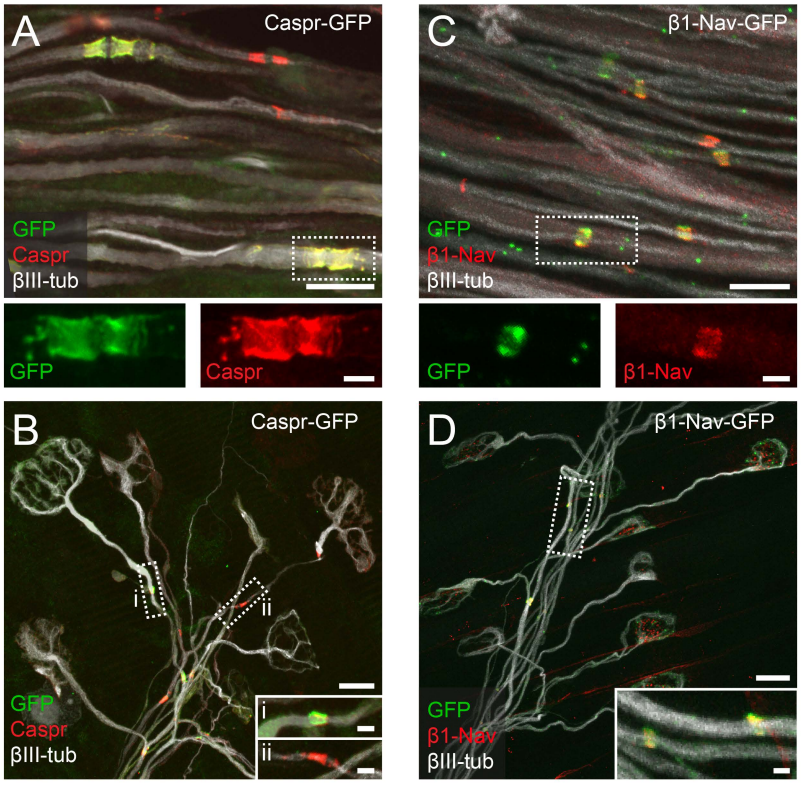

Wang et al., Figure S1

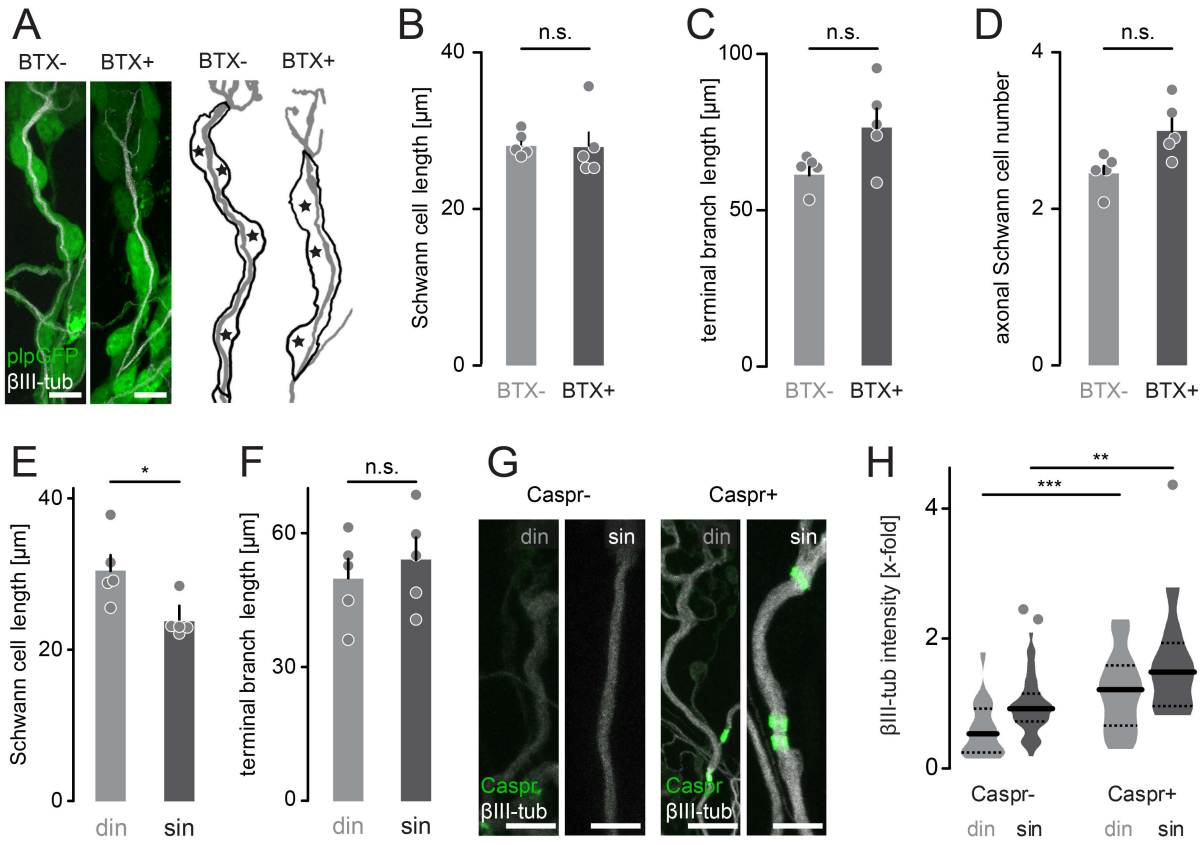

Wang et al., Figure S2

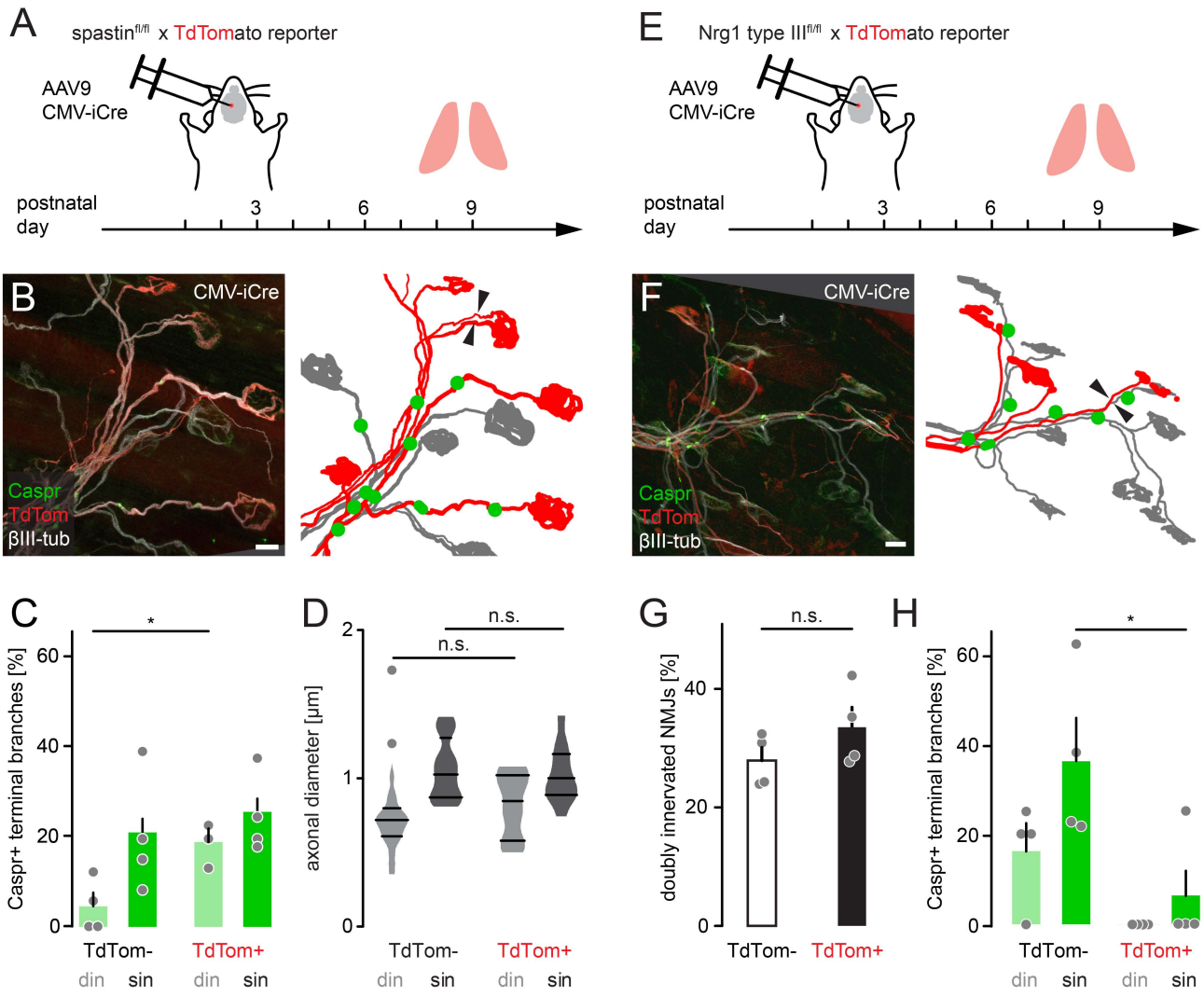

Wang et al., Figure S3

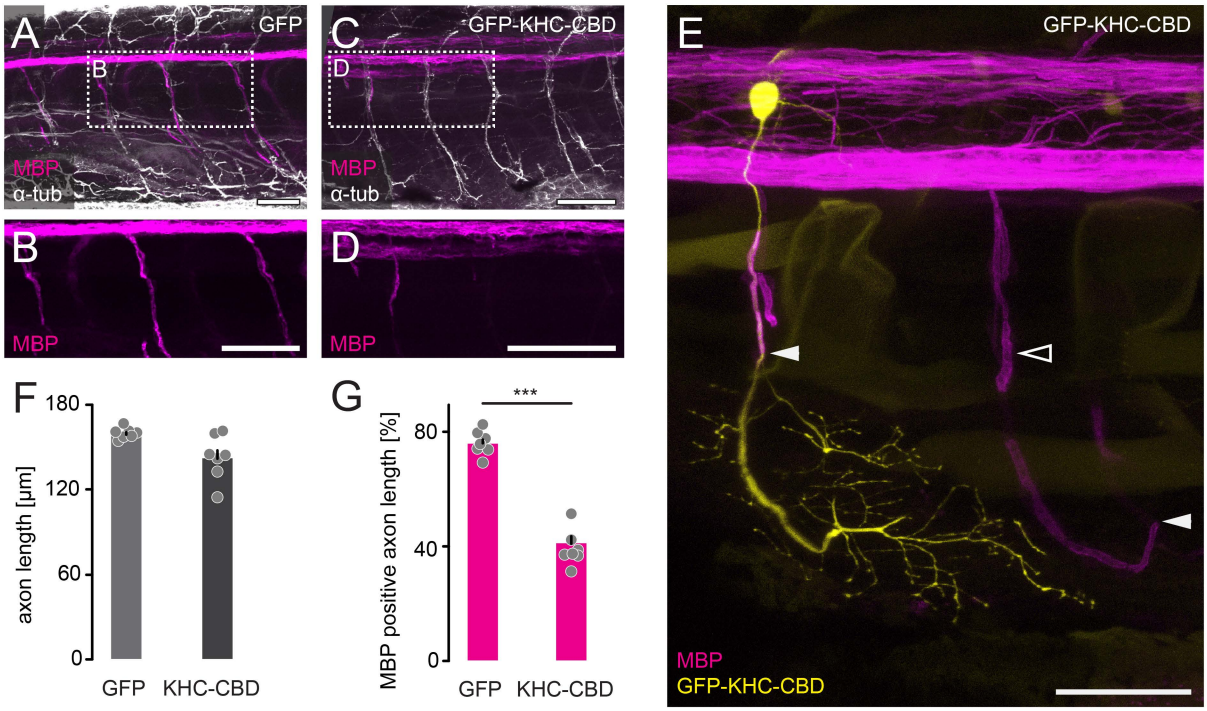

Wang et al., Figure S4